

**Academia Sinica Institute of Astronomy and Astrophysics
(ASIAA)
Summer Internship Program**

Project Title:
**“Near-Infrared Polarimetric Imaging of the
Protoplanetary Disk Around the T Tauri Star SU Aur”**

Jerome de Leon

Advisers:
Michihiro Takami, Ph.D.
Jennifer Karr, Ph.D.

July 1 – August 29, 2014
Taipei, Taiwan



TABLE OF CONTENTS:

CHAPTER 1

Introduction

Objectives of Study

CHAPTER 2

Observation

Data Reduction

Summary

Details (step by step)

CHAPTER 3

Preliminary Results

Observed PI Distribution

Disk Geometry and Orientation

Resolved Structures

Polarization Fraction

Radial PI Profile

Disk Model Simulations

CHAPTER 4

Analysis and Discussion

Nonaxisymmetric illumination of the disk in the inn

Asymmetric “spiral” structures

Tail associated with the disk

Disk Model Simulations

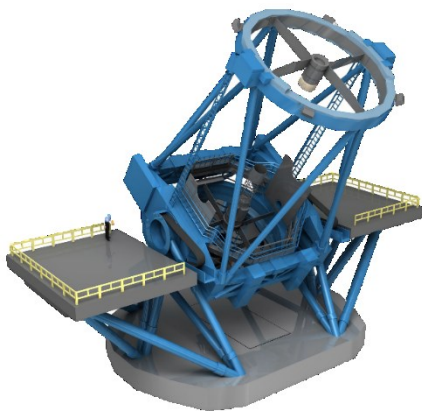
CHAPTER 5

Summary and Conclusions

Future Work

Acknowledgments

References



CHAPTER 1

INTRODUCTION

Direct imaging of protoplanetary/debris disks and exoplanets is challenging. In particular, the contrast in terms of brightness between the star and the disk around it range from $\sim 10^6 - 10^9$ in optical/ infrared wavelengths. A standard solution to overcome this problem is to implement coronagraphic imaging which significantly suppresses the stellar flux (and hence increases contrast of circumstellar environment) by blocking the direct starlight using a physical mask attached to the telescope.



Figure 1.0. Achieving high contrast imaging by implementing coronagraphic technique.

An alternative solution is to implement polarimetric imaging which filters out unpolarized starlight from the polarized starlight that reflected from the surface of the disk (see Watson et.al 2007, for a review). Polarized light refers to that in which the direction of oscillation of the electric field (or magnetic field) vector is random. In contrast, linearly polarized light is that in which the electric field (or magnetic field) vector is confined to a given plane along the direction of propagation.

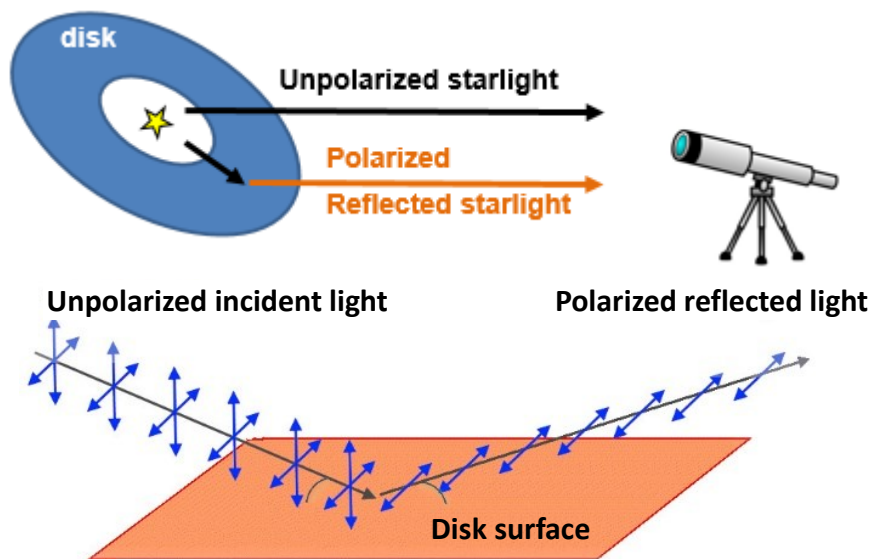


Figure 1.1. Top: Observed light from the star with disk around it can be polarized or not. Bottom: Unpolarized starlight becomes linearly polarized after it reflects from the surface of the disk.

Polarimetric imaging has been applied to a sample of stars known to have circumstellar disks. For example, HD 142527's circumstellar disk was inferred from near-infrared excess in its spectral energy distribution (SED). As shown below, this technique was able to reveal its complex disk structure that would have been undetected otherwise. Resolved images can only be obtained in limited circumstances in the optical and NIR, via an edge-on view or silhouette against bright background nebular emission (e.g., McCaughean et.al 2000, for a review).

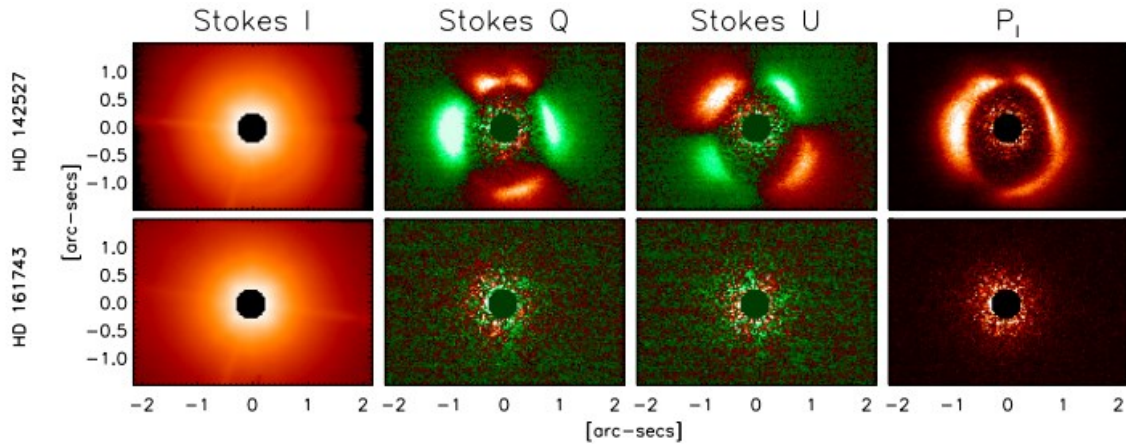
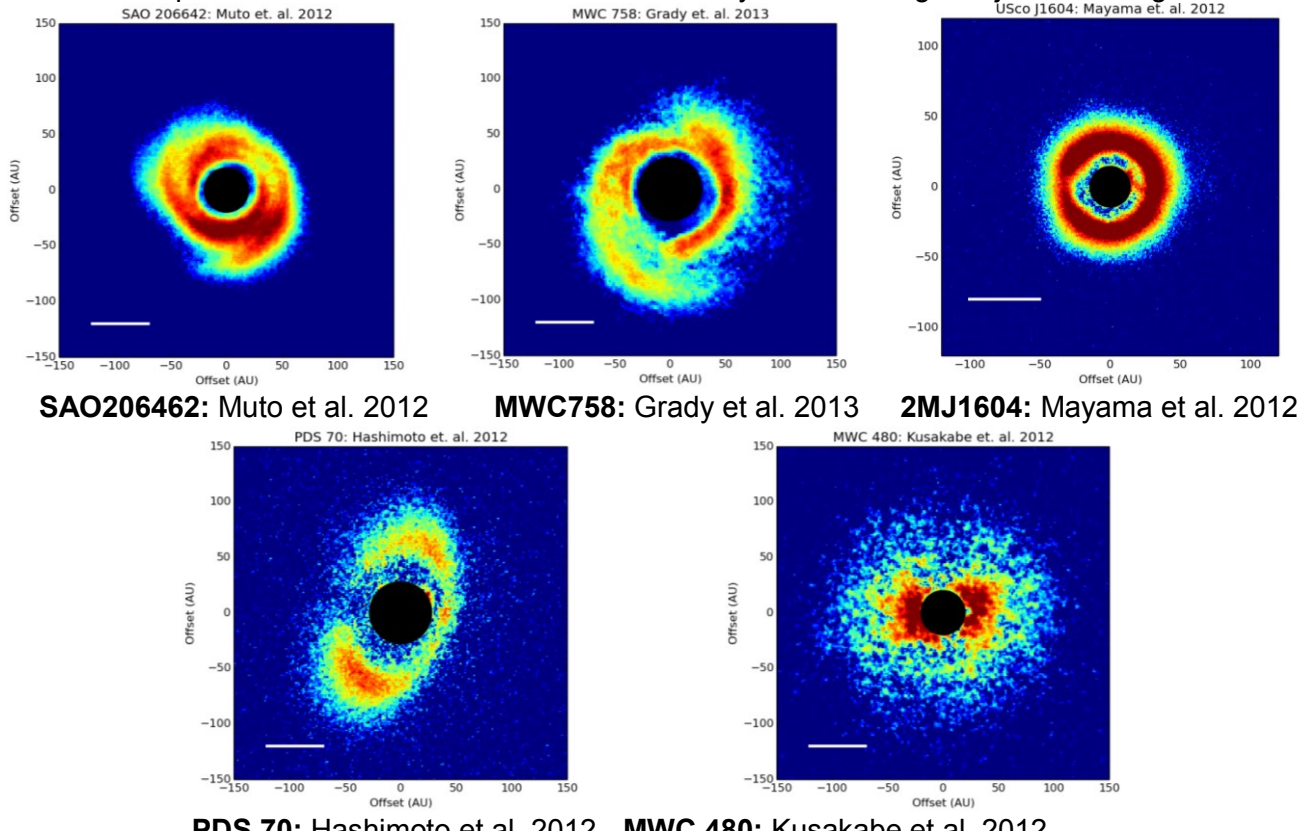


Figure 1.2. Processed images of HD 142527 (top row) and HD 161743 (bottom row) in H-band. From left to right: Intensity I image in logarithmic scale, Stokes Q, U, and PI images in linear scale. Saturated pixels have been masked out. Polarized images of top show a complex structure, while the comparison star shows only remnant noise. (Canovas et al. 2013)

This technique proved to be particularly successful as it was applied extensively during the direct imaging survey of exoplanets and disks using the 8-m Subaru telescope (SEEDS¹, Tamura 2009). Below are images of different young stellar objects (YSO) with protoplanetary disks showing diverse disk morphology that includes: spirals, gaps, rings, holes, and asymmetries. Resolving features in the disk is important because annular gaps and inner holes for example are believed to be due to dynamical interaction between the planet and the disk providing hints of on-going planet formation. These PI images in the SEEDS sample will be used later to compare with the results obtained from the analysis of our target object SU Aurigae.



PDS 70: Hashimoto et al. 2012 MWC 480: Kusakabe et al. 2012
Figure 1.3. Five best SEEDS imaged disk samples that exhibit diverse disk morphologies.²

¹ Strategic Exploration of Exoplanets and Disks with Subaru

² credit: The SEEDS team

SU Aurigae

SU Aurigae (hereafter SU Aur) is a classical T Tauri star (Herbig 1952; Giampapa et al. 1993; Bouvier et al. 1993) and is a member of the Taurus-Auriga star-forming region, with a distance of ~ 140 pc (Bertout & Genova 2006). A summary of SU Aur's stellar parameters is given in Table 1.1. It is classified as G2 subgiant with an exceptionally fast rotation $v \sin i = 66$ km/s and is one of the brightest classical T Tauri stars with $V=+9.16$ mag and $(B-V)=+0.90$. SU Aur is also characterized by strong photometric variability caused by dark starspots and bright accretion hotspots (DeWarf et al. 2003). SU Aur has been the target of many studies at all wavelength ranges, though these were primarily focused on understanding the central star and not its large-scale circumstellar environment. Observational signatures of a circumstellar disk are present in SU Aur's infrared and UV excess (Bertout et al. 1988; Kenyon & Hartmann 1995) and in spectroscopic observations that show optical veiling from circumstellar and/or accreting material (Unruh et al. 2004).

The innermost region of SU Aur's circumstellar disk have been resolved using long-baseline interferometry from the Palomar Testbed Interferometer (Akeson et al. 2002, 2005). These observations are most sensitive to the hot disk material that is close to the star, resulting in a reliable determination of the inner disk radius (0.13 or 0.18 AU depending on whether the model is face-on or inclined (Akeson et al. 2005). Additionally, Akeson et al. (2002, 2005) determined SU Aur disk's inclination to be 62° . This matches the inclination of stellar rotation of $50\text{--}70^\circ$ measured using the tomographic Doppler imaging by Unruh et al. (2004). Jeffers et al. (2013) carried out optical polarimetric imaging of the circumstellar environment of SU Aur and found very small grains in the surface layers of the SU Aur's disk. Their images resolved a large extended nebulosity that is argued as a remnant of the prenatal molecular cloud because of the position angle of the disk and the brightness of the nebulosity. Jeffers et.al. (2013) argue that their study rules out the previous speculation of a cavity carved out by a jet.

Table 1.1. Stellar parameters of SU Aur*

Parameter	Value	Reference(s)
Spectral Type	G2 III	1
Mv	9.16 Mag	2
B-V	+0.90	2
T (Effective)	5860 ± 100 K	3
Mass	$1.88 \pm 0.1 M_\odot$	3
Radius	$3.5 R_\odot$	4
$v \sin i$	66 km/s	5, 6
Age (log t)	6.8 ± 0.08 yr	7
Luminosity	$9.29^{2.26}_{-1.65} L_\odot$	3
Inclination	63^{+4}_{-8} degrees	8
Distance	143 pc	9
Av	0.9 mag	3

(1) Herbig (1952); (2) DeWarf et al. (2003); (3) Bertout et al. (2007); (4) Muzeirole et al. (2003); (5) Johns-Krull (1996); (6) Unruh et al. (2004); (7) Bertout et al. (2007); (8) Akeson et al. (2002); (9) Bertout & Genova (2006). The stellar coordinates are taken from Simbad (<http://simbad.u-strasbg.fr>).

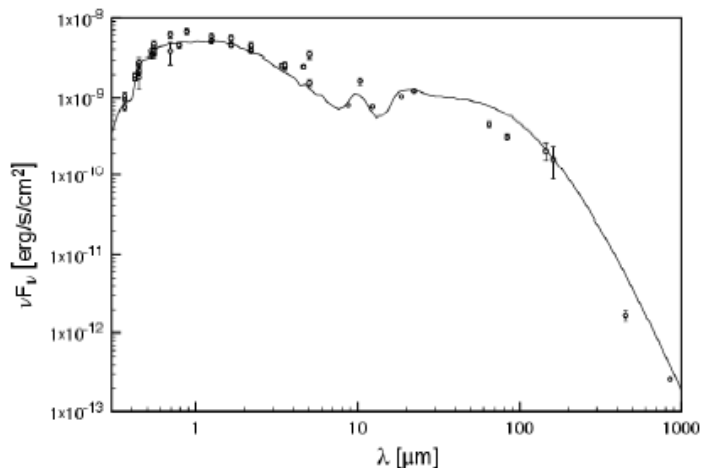


Figure 1.4. SED of SU Aur* (*Jeffers et al. 2013)

Objectives

The aim of this project then is to investigate the morphology of SU Aur disk in the NIR using polarimetry to probe its inner, unexplored regions, and derive relevant physical properties. Originally, it was also aimed to carry out simulation using conventional disk models to reproduce the observed morphology of SU Aur and hence constrain its disk and dust parameters.

CHAPTER 2

OBSERVATION

We carried out polarimetry in H-band ($1.65 \mu\text{m}$) toward SU Aur using the high resolution imaging instrument HiCIAO (Tamura et al. 2006; Hodapp et al. 2006) with a dual-beam polarimeter mounted on the Subaru 8.2 m Telescope on January 19, 2014. These observations are part of the ongoing SEEDS survey. The adaptive optics system (AO188; Hayano et al. 2004; Minowa et al. 2010) provided a stable stellar point spread function (PSF, FWHM = $0.^{\circ}08 \sim 8$ pixels). We employed a spectral differential imaging (SDI) mode in which a dual Wollaston prism was used to split incident light into two pairs of images that are linearly polarized on orthogonal planes, each with a $5'' \times 5''$ field of view and a pixel scale of 9.5 mas/pixel.

As with several other SEEDS observations, Stokes parameters I, Q, and U were measured by rotating the half-wave plate to four position angles (PAs) from 0° , 45° , 22.5° , and 67.5° in sequence. We obtained 12 full waveplate rotation cycles, taking a 30-sec exposure per waveplate position, using 10% neutral density (ND) filter and without a coronagraphic mask in order to image the inner most region around the central star. Additional 4 sets of waveplate cycles this time using 1% ND filter were obtained for aperture polarization. These were also used to measure the PSF FWHM and total stellar flux (hereafter I^*). The angle of total field rotation was $\sim 52^\circ$ during the observations. The total integration time of the polarized intensity (P/I) image was (12 sets \times 4 PA \times 30-sec =) 1440-sec considering all quality images with small FWHMs (FWHM $< 0.^{\circ}.1$) by careful inspections of the stellar PSF.

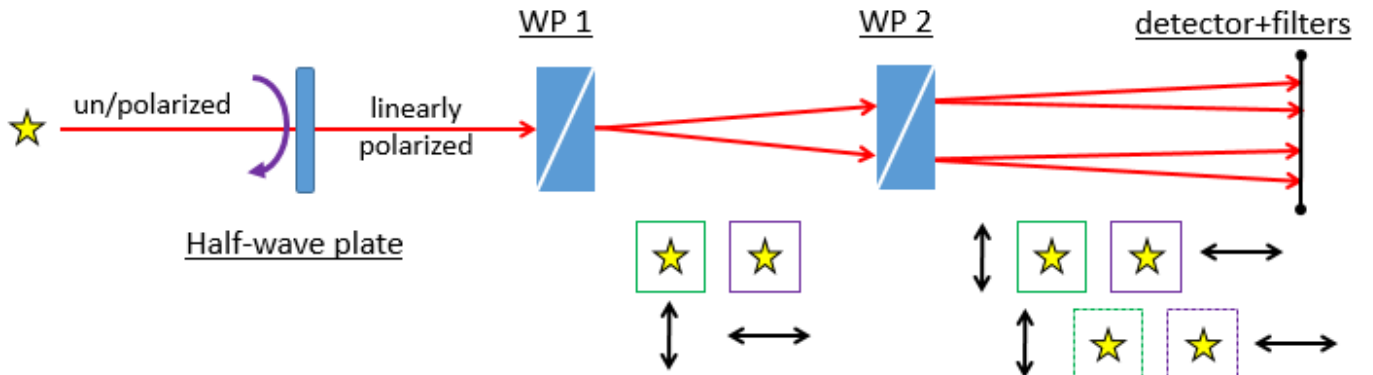


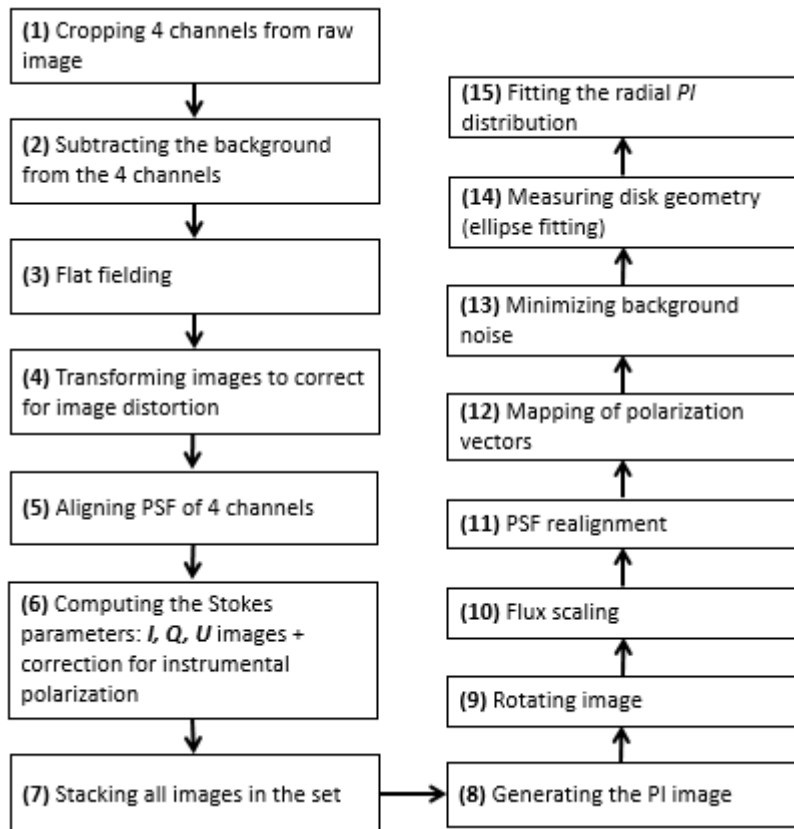
Figure 2.0. HiCIAO configuration in SDI mode consisting of: half-wave plate used to rotate the polarization direction of then polarized light; and Wollaston prism to separate the incoming beam into 2 orthogonal linearly polarized light.

DATA REDUCTION

Summary of Data Reduction

The data was reduced using a combination of angular, spectral, and polarimetric differential imaging (ADI+SDI+PDI). The raw images were corrected using self-written codes in python to correct for dark current and flat-field following the standard reduction scheme. We applied a distortion correction using IRAF packages GEOMAP and GEOTRAN. Stokes Q and U parameters and the PI image were obtained in the standard approach (e.g., Hinkley et al. 2009) as follows. By subtracting two images of extraordinary- and ordinary-rays at each wave plate position, we obtained $+Q$, $-Q$, $+U$, and $-U$ images, from which $2Q$ and $2U$ images were made by another subtraction to eliminate remaining aberration. The measured Stokes I, Q, and U

parameters were used to compute the more accurate, intrinsic Stokes I, Q, and U (Hashimoto et.al 2011). Finally, the PI image was derived by using the equation $\text{PI} = \sqrt{Q^2 + U^2}$ and the angle of polarization using $\theta_{\text{PI}} = 0.5 \times \arctan(U/Q)$. The data reduction pipeline is shown in the flowchart below.



Flowchart 2.0. Data reduction pipeline for SU Aur.

I. Details of Image Processing of SU Aur

Observation log file (see *Obs_log140119.pdf* & *log_all.txt*) summarizes the observation settings of SU Aur science images. The science images in fits file format are divided into three groups including the (1) object itself imaged using 10% neutral density (ND) filter (hereafter ND10), (2) the same object with 1% ND filter (ND1), and (3) the reference star (ref) with 10% ND filter also. The images in all the groups were imaged without coronagraphic mask. In each group, images are further divided in sets. One set contains images with different half-wave plate position angles (PA's). For example, image id = (120,121,122,123) correspond to PA = (0°, 45°, 22.5°, 67.5°). In total, there are 96 images or 24 half-wave plate cycles. Refer to Table 2.1. for full image settings.

Table 2.1. Summary of observation log

	Object	File i.d. (half-wave plate set)	Exposure time	Category	filter transmission	Alias
1	SU Aur	HICA00137+ 120-131 (3 sets) 223-226 (1 set)	15 s	aperture polarization (ap. pol.)	1%	ND1
2	SU Aur	132-171 (10 sets) 215-222 (2 sets)	30 s	science	10%	ND10 or obj
3	HD241730 (Reference star)	240-271 (8 sets) TOTAL: 96 (24 sets)	20 s	science	10%	ref

A sample science image (raw form) shows four bright sources. All of the four “channels” correspond to the same object, SU Aur, imaged simultaneously with ND filter centered at ~1.6 microns (H-band) in the infrared part of the electromagnetic spectrum. Each channel have a 5 square arc-seconds ($5'' \times 5''$) field of view. Artifacts, such as horizontal stripes among others, are evident in the image. These are caused by instrumental errors and must be corrected by means of image reduction and processing. The detailed procedure is explained as follows.

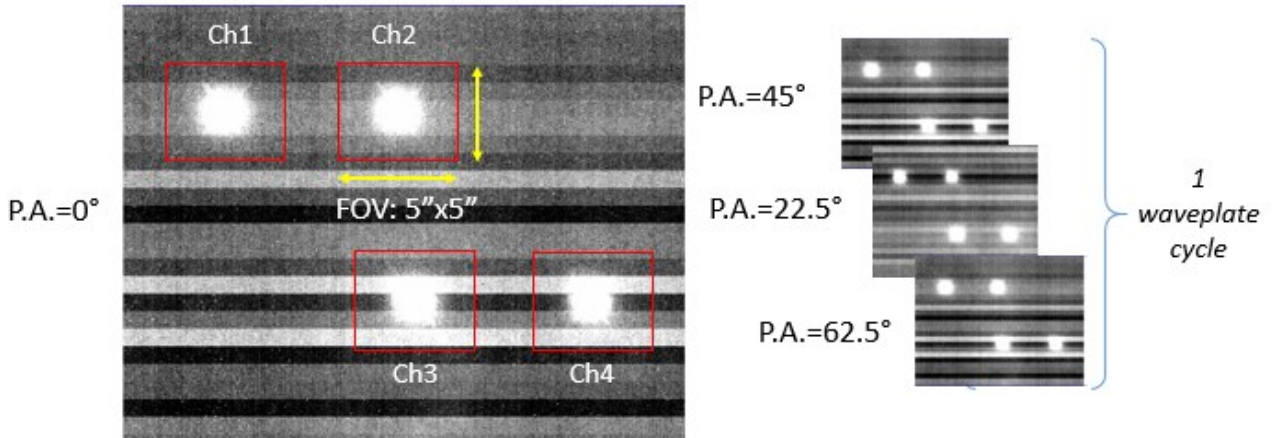


Figure 2.1. Sample images for a half wave-plate cycle (file i.d.: 132, 133, 134, and 135 corresponding to successive P.A.’s).

>STEP 1: Cropping channels

The four channels were extracted from each raw image by utilizing IRAF’s imcopy command. The detailed description of the program is explained in the python program (see *1cropping.py*). The output images are named ‘HICA*_ch1.fits’ found in the *channels* folder. Sample images of extracted channels in each group are shown below.

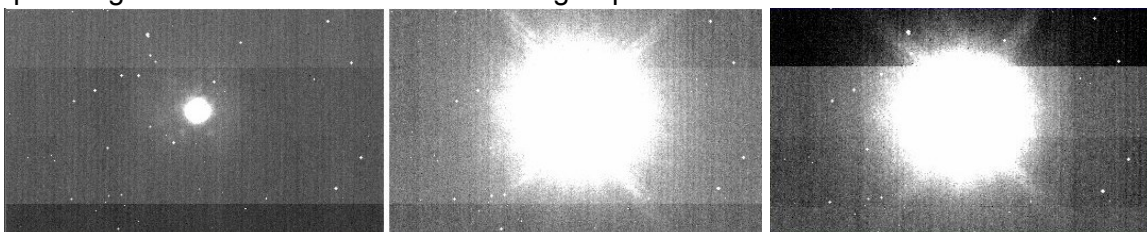


Figure 2.2. Channel 1 of the raw ND1, ND10, and ref images (id= *120, *132, and *240, then renamed as 120_ch1, 132_ch1, and 240_ch1), from left to right respectively

>STEP 2: Background subtraction

Background subtraction is necessary to minimize, if not eliminate, the random noise in the raw images caused by the inherent errors in detector and other factors. This was done by taking the median of the cropped image excluding the bright central source and subtracting it from the image itself (see *2test_median_all.py*). The output images are named as ‘HICA*_ch1b.fits’ found in the *bg_sub* folder. A sample of resulting images are shown below. In this step alone, the erroneous stripes have been removed.

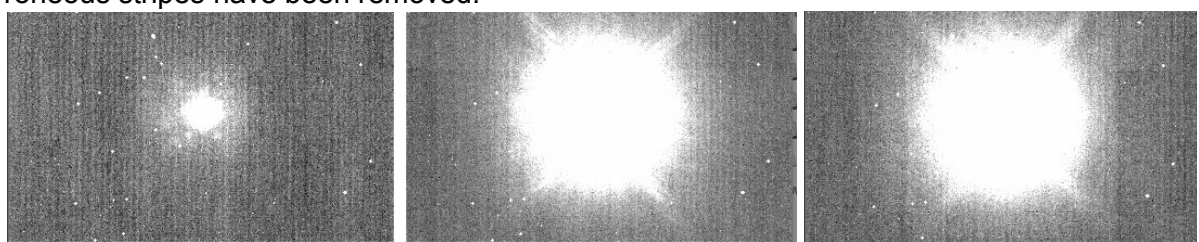


Figure 2.3. 120_ch1, 132_ch1, and 240_ch1 after background subtraction (now 120_ch1b, 132_ch1b, and 240_ch1b)

>STEP 3: Flat fielding

Flat fielding is needed to remove artifacts in the image caused by variations in the pixel-to-pixel sensitivity of the detector and/or by distortions in the optical path. This was done by dividing the noise-subtracted image by a given flat image (i.e. image of an evenly illuminated field) of the corresponding channels. The output images are named as ‘HICA*_{ch1bf.fits}’ found in the *flat* folder (see *3test_flat.py*). The resulting sample images are shown below.

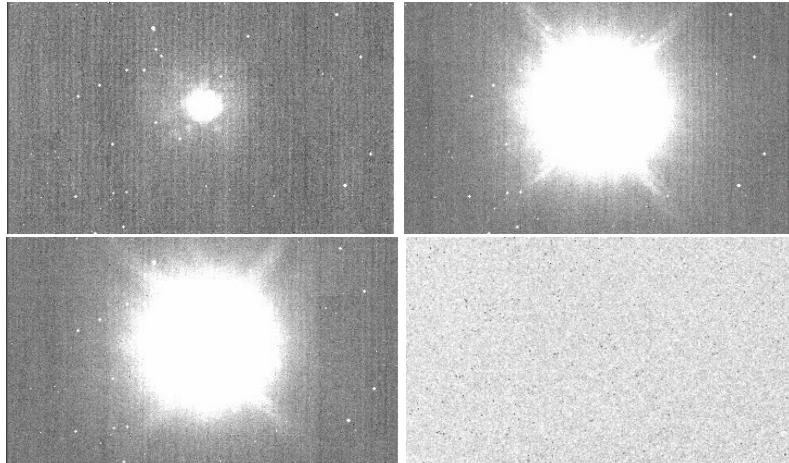


Figure 2.4. 120_ch1b, 132_ch1b, and 240_ch1b after flat fielding (now 120_ch1bf, 132_ch1bf, and 240_ch1bf). The last frame is the flat image for channel 1 (flat_ch1).

>STEP 4: Image distortion correction

Image transformation is need to correct for geometrical distortion caused by imperfections in the optics. This was done by utilizing IRAF’s GEOTRAN command and applying it to each channel specified by the given database files (e.g. ch1_Jan2014.db and ch1_Jan2014.dat) which provided the desired coordinate transformations. The .db file was produced by GEOMAP (see *geom_transform.py*). The output images are named as ‘HICA*_{ch1bfg.fits}’ found in the *im_distort* folder. The resulting sample images are shown below.

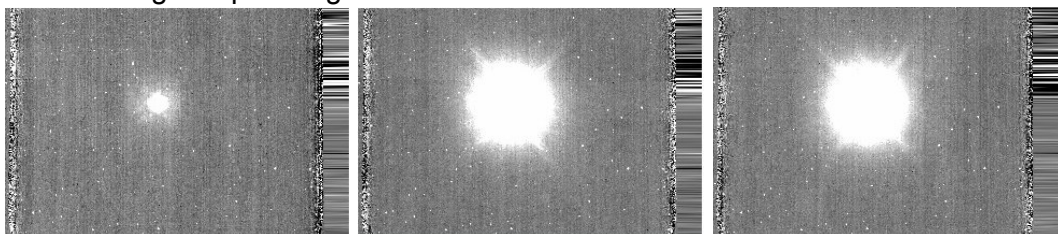


Figure 2.5. 120_ch1bf, 132_ch1bf, and 240_ch1bf after geometric distortion correction (now 120_ch1bfg, 132_ch1bfg, and 240_ch1bfg). The frames are zoomed out for clarity. The stripes on the right part of each frame are artifacts caused by image transformation.

>STEP 5: PSF alignment

Alignment of paired channels (i.e. ch1 & ch3 and ch2 & ch4) is necessary to make sure that stacking will yield correct results. This was done by first inspecting whether the point spread function (PSF) of each channel pairs of a given half-wave plate P.A. will subtract perfectly yielding fewest residual light. Otherwise, the channels would be shifted relative to a predefined image center. The output images are found in the *align* folder (see *5test_align.py* & *5bulk_align.py*). Sample images are shown below.

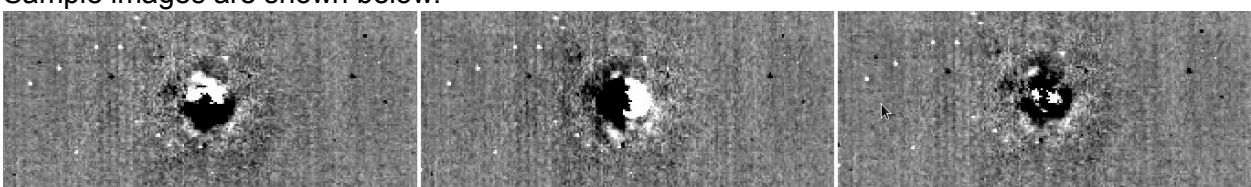


Figure 2.6. (a) ch1 and ch3 subtraction showing alignment in x-axis; (b) same channels aligned in y-axis (c) same channels aligned in both x- and y-axes; same process is done to ch2 & ch4

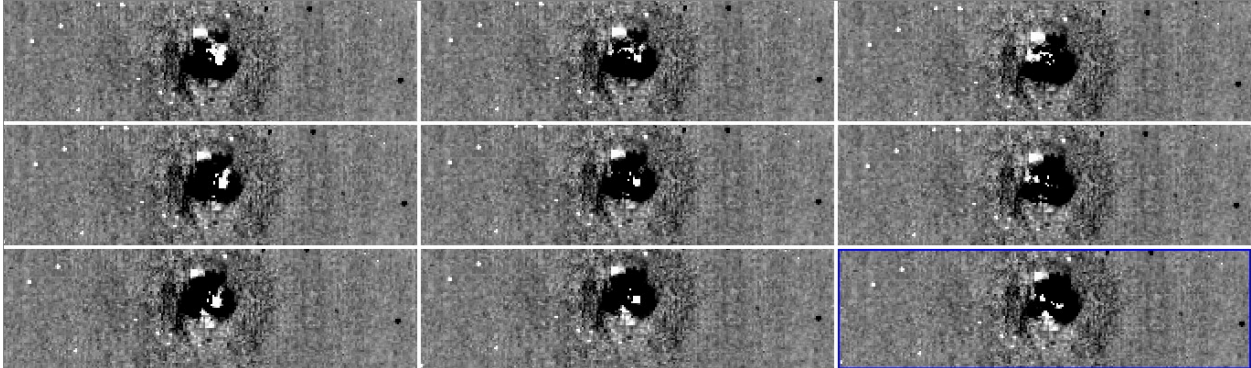


Figure 2.7. Images generated when a single image was shifted in both x and y directions by a few pixels; the image in the center frame shows best PSF subtraction determined by trial and error.

>STEP 6: Computing the Stokes parameters

The Stokes parameters (denoted I , Q , U) are a set of values that describe the polarization states of the observed radiation. They are defined as follows.

Observed Stokes parameters

$$I = (\text{ch1} + \text{ch3}) + (\text{ch2} + \text{ch4}) = o + e$$

$$Q = I_0 - I_{45}$$

$$U = I_{22.5} - I_{67.5}$$

where the subscript denotes the half-wave plate P.A. The first pair (ch1 & ch3) is also referred as the ordinary ray or o-ray and the second pair (ch2 & ch4) is referred as the extraordinary ray or e-ray. In essence, the I image is the total integrated intensity of all channels in a given P.A. The calculation of Q and U images then correspond to the subtraction of two orthogonal integrated (unpolarized) stellar PSF.

It is convenient to define another parameter called the oe-ray which is defined as the difference of the individual o- and e-rays. In contrast, the I image is the sum of the o- and e-rays. The output I images are found in the *OE* and *I_corrected* folders (see *6oe_I.py* and *test_oe.py*).

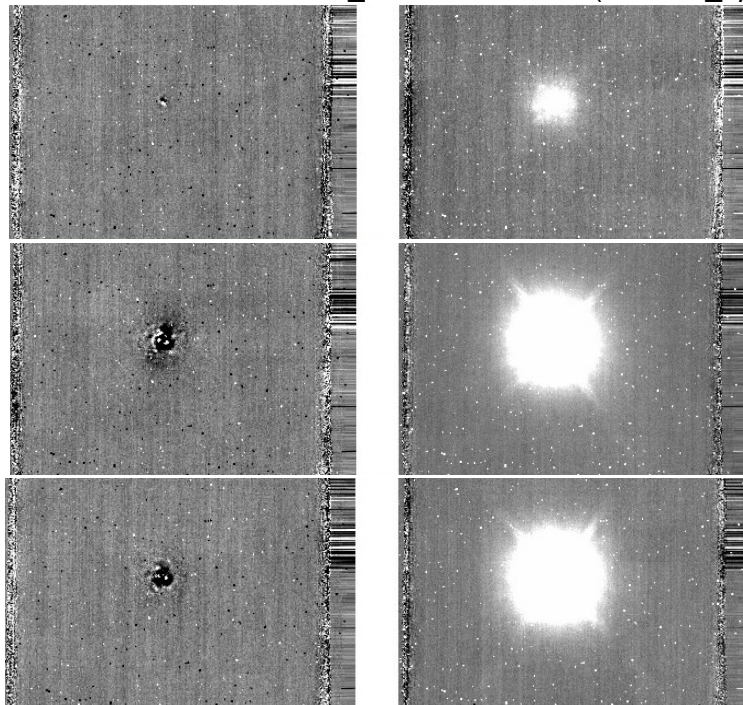


Figure 2.8. top row: 120_oe and 120_I; middle row: 132_oe and 132_I; bottom row: 240_oe and 240_I (120,132, and 240 all correspond to P.A.=0°).

Note that there were no images presented for the “observed” Q and U using the above equations. Instead, a set of more accurate equations describing the “intrinsic” Stokes Q and U was used. The equations were provided by Jun Hashimoto-san. They are described below.

More accurate Stokes I , Q and U

Previously, Stokes I was computed by simply adding o- and e-rays. A more accurate I can be obtained by averaging the intensity of all channels over the entire wave plate cycle:

$$I = \frac{(I_0 + I_{45} + I_{22.5} + I_{67.5})}{4}$$

This then improves measurement of Stokes Q and U parameters.

Another feature of these equations is accounting for instrumental polarization. The technique developed by Joos et al. (2008) was adapted in this study and explained as follows. A given text file (see *IP_SUAur_20140119.txt*) containing the constants referred to as X_{ij} was used to compute for corrected I , Q and U . From left to right, the columns ($=X_{ij}$) in the .txt file are denoted as: `image_no`, `x11`, `x12`, `x13`, `x14`; `x21`, `x22`, `x23`, `x24`. Thus, equation for I that corrects for instrumental polarization becomes:

$$I \sim \sum_j \frac{[o_j + e_j]}{x_{11;j}} / 4$$

where $j = \{0, 45, 22.5, 67.5\}$. This simply divides the `x11` (constant) value of a given half-wave plate P.A. to previously computed I image and doing this for the entire set. For example, the I image generated using the first half-wave plate set: 120, 121, 122, and 123 can be computed using

$$I_{\text{cor}} = \frac{\left(\frac{120_I}{120_x11} + \frac{121_I}{121_x11} + \frac{122_I}{122_x11} + \frac{123_I}{123_x11} \right)}{4}$$

The resulting image is named `120-123_I`.

The values of X_{ij} are also important in incorporating corrections in the intrinsic Q and U parameters by computing the constants a, b, c, d and p, q, r, s which eventually yield the Q and U images as described below.

$$Q \sim \frac{\left(\frac{a}{d} - \frac{p}{s} \right) - \left(\frac{b}{d} - \frac{q}{s} \right) * I}{\frac{c}{d} - \frac{r}{s}} \quad \text{and} \quad U \sim \frac{a - b * I - c * Q}{d}$$

where

$$a = [o(0^\circ) - e(0^\circ)] - [o(45^\circ) - e(45^\circ)] \quad (\text{e.g. } 120_oe - 121_oe)$$

$$b = x_21(0^\circ) - x_21(45^\circ)$$

$$c = x_22(0^\circ) - x_22(45^\circ)$$

$$d = x_23(0^\circ) - x_23(45^\circ)$$

$$p = [o(22.5^\circ) - e(22.5^\circ)] - [o(67.5^\circ) - e(67.5^\circ)] \quad (\text{e.g. } 122_oe - 123_oe)$$

$$q = x_21(22.5^\circ) - x_21(67.5^\circ)$$

$$r = x_22(22.5^\circ) - x_22(67.5^\circ)$$

$$s = x_23(22.5^\circ) - x_23(67.5^\circ)$$

Note that a, p, I = matrices and b, c, d, q, r, s = constants (see *7IP_test.py* that manually computes for corrected I including Q and U images; see *7Icor_set.py* that automatically computes for corrected I images only; see *8UQ_set.py* that automatically computes for sets of Q and U images). The output images are named `*_Q` and `*_U` found in the `QU` folder with 3 subfolders containing the output in each image set. Sample images are shown below.

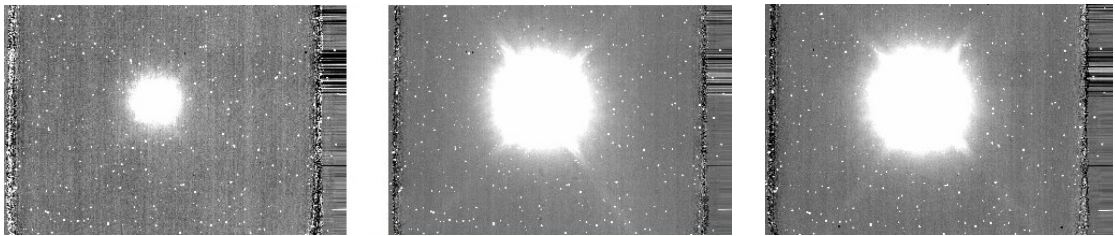


Figure 2.9. Corrected I images for the sets 120-123, 132-135, and 240-243.

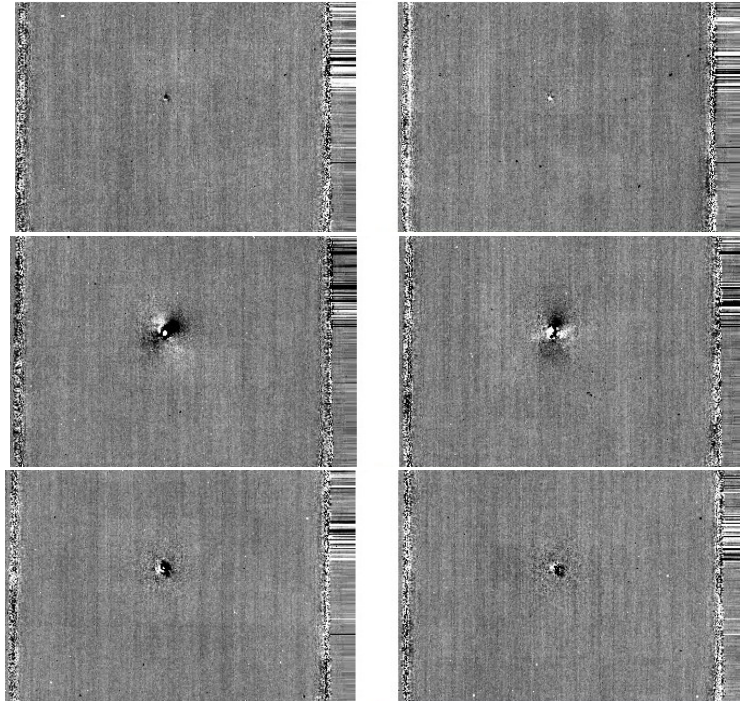


Figure 2.10. top row: 120-123_Q and *_U; middle row: 132-35_Q and *_U; bottom row: 184-187_Q and *_U. The Q and U images of the object shown in the top row (ND1) are underexposed. Therefore, the following analysis will only focus on the ND10 images of the object.

Note that the output filenames adapted a new naming convention of 120 up to 212 (instead of original 120-171, 216-223, and 240-271) removing gaps in i.d. number to make automated naming in the python programs work. The changes are highlighted in the table below.

Table 2.2. Change of file id.

	Old file i.d. HICA00137+	New file i.d. HICA00137+
1	120-131 (3 sets) 223-226 (1 set)	same 180-183
2	132-171 (10 sets) 215-222 (2 sets)	same 172-179
3	240-271 (8 sets)	184-211

>STEP 7: Image rotation

Rotating the corrected intensity images and Q and U images by an angle fr is needed to account for field rotation during observation. By rotating the images, they will be aligned from a common point (image center) and hence makes stacking more reliable. The files were saved as *_rotl.fits. The first set of images: 120-171 inclusive → 13 image sets

<ND1> 120, 124 128

<ND10> 132, 136, 140, 144, 148, 152, 156, 160, 164, 168

The field rotation angle for SU Aur is $\sim 44^\circ$ and $\sim 52^\circ$ for reference star. The field rotation angles are different between exposures because of use of the ADI mode. The output images are

named as *_rotl, *_rotQ, and *_rotU found in the *rotated_QU* folder. Sample rotated *I* and *Q* and *U* images are shown below.

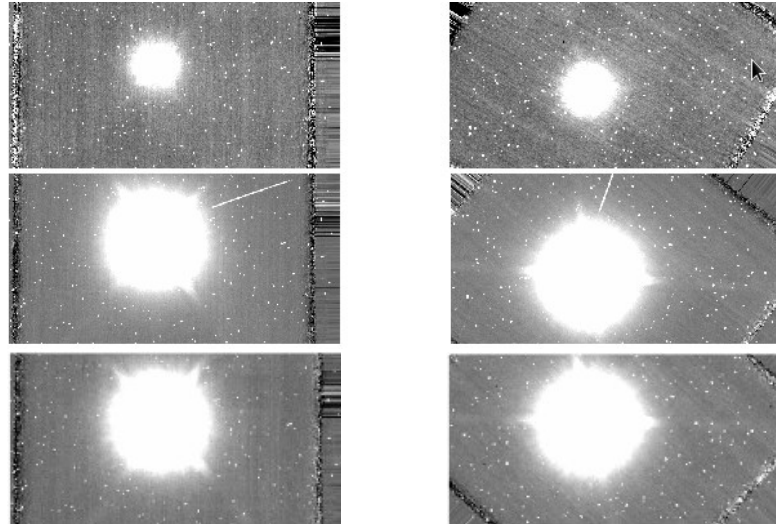


Figure 2.11. Left column: before; Right column: after rotation of the *I* images.
Row 1: 120-123_rotl (ND1); Row 2: 168-171_rotl (obj); Row 3: 208-211 (ref).

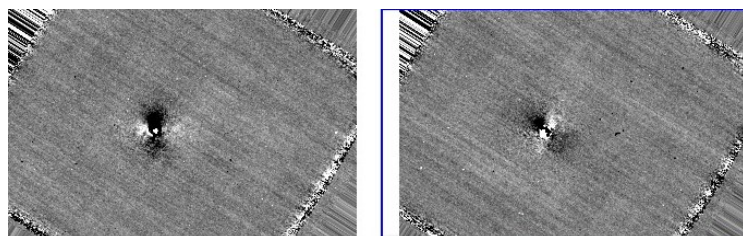


Figure 2.12. Left: 132-135_rotQ and *rotU images of the object.

>STEP 8: Stacking

This step entails stacking the groups of images in each set (obj/ND10, ND1 and ref) to increase signal to noise ratio. Using the rotated images, the task is simply to calculate the median in each pixel in the images in the entire set (e.g. median of all obj images) to make a "stacked image" (see *9median_I_set.py* and *9median_QU_set.py*). There are 2 outputs for each set: obj_medI, and obj_medQ & obj_medU; ref_medI and ref_medQ & ref_medU; and ND1_medI and ND1_medQ & ND1_medU. The outputs are found in the *stacked* folder.

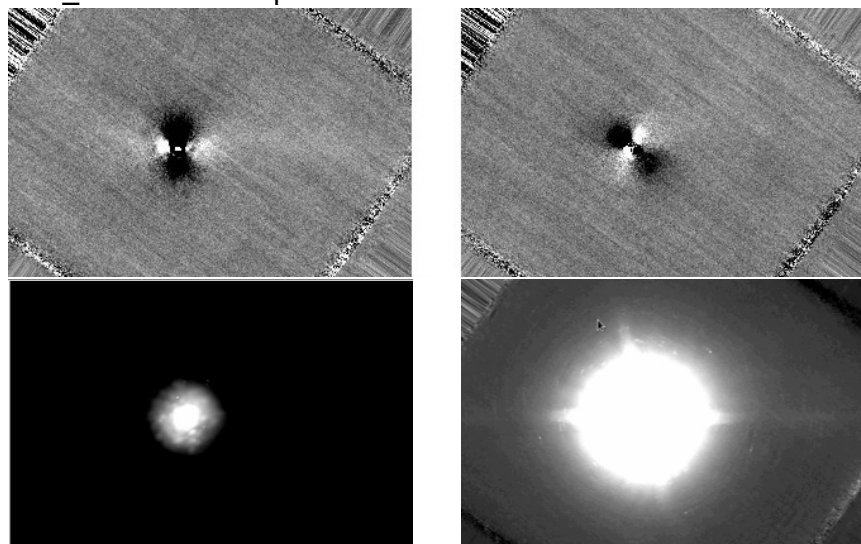


Figure 2.13. Top row: Q (left) and U images (right) of SU Aur after stacking (obj_medQ and obj_medU); Bottom row: Intensity images of the object after stacking (obj_medI). The two

images are identical except in their contrast. There were no obvious signs of disk structure around the bright star.

>STEP 9: Generating PI images

This step entails generating the polarized intensity (PI) image of SU Aur (using ND1 and ND10 and also ref data set). The PI image and direction of polarization is computed using the Stokes Q and U parameters:

$$PI = \sqrt{Q^2 + U^2}$$

$$\theta_{PI} = 0.5 \tan^{-1}(U/Q)$$

The Q and U images in Fig. 2.13 were used to generate the PI image of the object (obj_PI). This is done by first by importing *_medQ and *_medU and using them as inputs (see *test_PI.py* and *PI_set.py*). The resulting image is shown below.

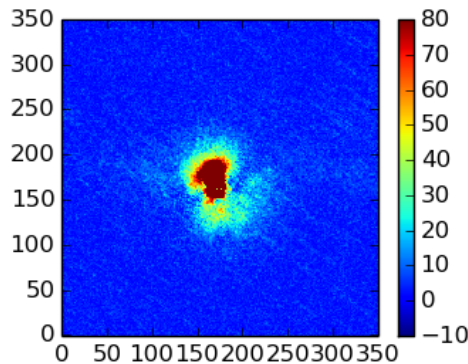


Figure 2.14. Polarized Intensity (PI) image of SU Aur presented in default ‘jet’ colormap plotted using the pyplot library. Note that there are different sets of PI images generated using ND1 and ref (not shown here). The x- and y-axes are in pixels and color bar denotes flux level in PI.

>>Convolution and Optimization of parameters

Convolution using a 2D Gaussian PSF was done to smoothen the image. Smoothing using a Gaussian function is also called Gaussian blur. Gaussian (normal) distribution in 2D is written as:

$$f(x, y) = \frac{1}{2\pi\sigma^2} \exp\left(-\frac{x^2 + y^2}{2\sigma^2}\right)$$

where σ is the standard deviation.

Different color maps (gray, spectral, jet, and hot), and vmin/vmax scales were used to increase the contrast and reveal features in the current PI and convolved images. There were two output images (PI and PI_conv) per set (obj_*, ref_*, ND1_*). Interesting features in the rotated PI image include:

- (1) Long tail extending to the right of the image,
- (2) Pair of possible spiral arms, and
- (3) Dips/ asymmetries in the inner part of the disk

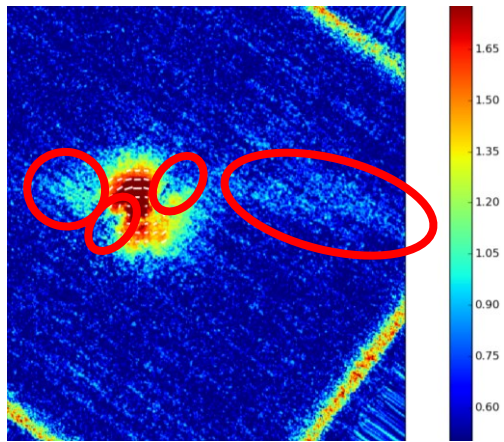


Figure 2.15. Interesting features revealed in the object's convolved PI image.

It was later found out that using `cmap=jet`, `vmin/vmax= -7/ -5` for convolved images with `sigma =2` in log stretch, and using Gaussian filter for interpolation were the optimum parameters.

>>>Relationship between standard deviation, σ , and FWHM

$$\text{FWHM} = 2\sqrt{2 \ln 2} = 2.355 \sigma$$

This is used to determine the maximum sigma that can be used for convolution such that it would not alter the original signal:

$$5 \text{ pixels} = 2.355 \sigma$$

$$\sigma = \frac{5 \text{ pixels}}{2.355} = 2.12$$

The value of $\sigma = 2$ is used in convolution (or smoothing) of images using Gaussian filter. Resulting convolved images with different sigma are shown below. The images' axes are now scaled in AU (scale conversion is shown in the Appendix, see `10PI_set.py`)

>STEP 10: Flux scaling

This step entails normalizing the flux of the `obj_PI` relative to the stellar / flux. As the stellar flux is saturated in the science frames (ND10, exposure time 30 s), it was alternatively measured from the ND1 images and exposure time of 15s. IRAF's photometry module called `phot` (saved in the `ND1_mdel_a.fits.mag.1`) was used, and the flux was 1,711,181 ADU. The stellar flux for the science frames was computed as follows:

$$\text{obj_PI_fs} = \frac{\text{obj_PI}}{\text{stellar_flux}}, \text{ where}$$

`stellar_flux`=measured `ND1_flux`*(`ND10/ND1` exposure time ratio)*(`ND10/ND1` flux ratio). Here, the exposure time is `30s/15s = 2` and the flux ratio is 10. So basically, a constant (=20) is multiplied to the `ND1` flux to get the stellar / flux. Dividing this value from the `PI` image of the object yielded the normalized flux which is in the order of $\sim 10^{-6}$. The outputs are (e.g. `obj_PI_fs.fits`) found in the `flux_scaling` folder (see `11PI_flux_scaling.py`).

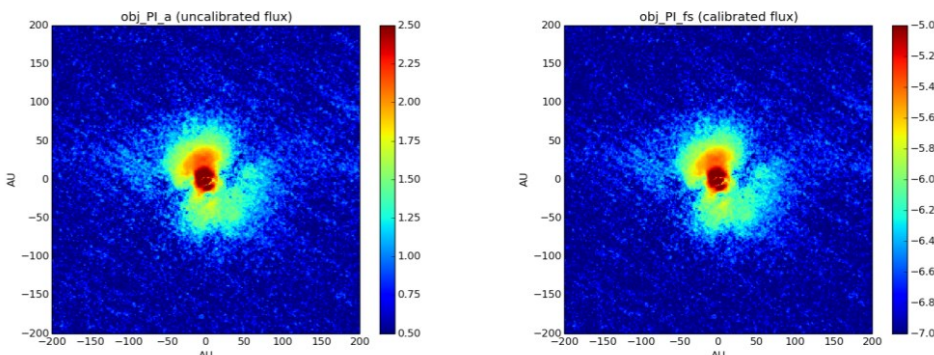


Figure 2.16. Left: PI image before flux scaling; Right: PI image after flux scaling (PI/I_*). The overall distribution is preserved except the flux values on the right are much smaller as shown by the scale (i.e. colorbar).

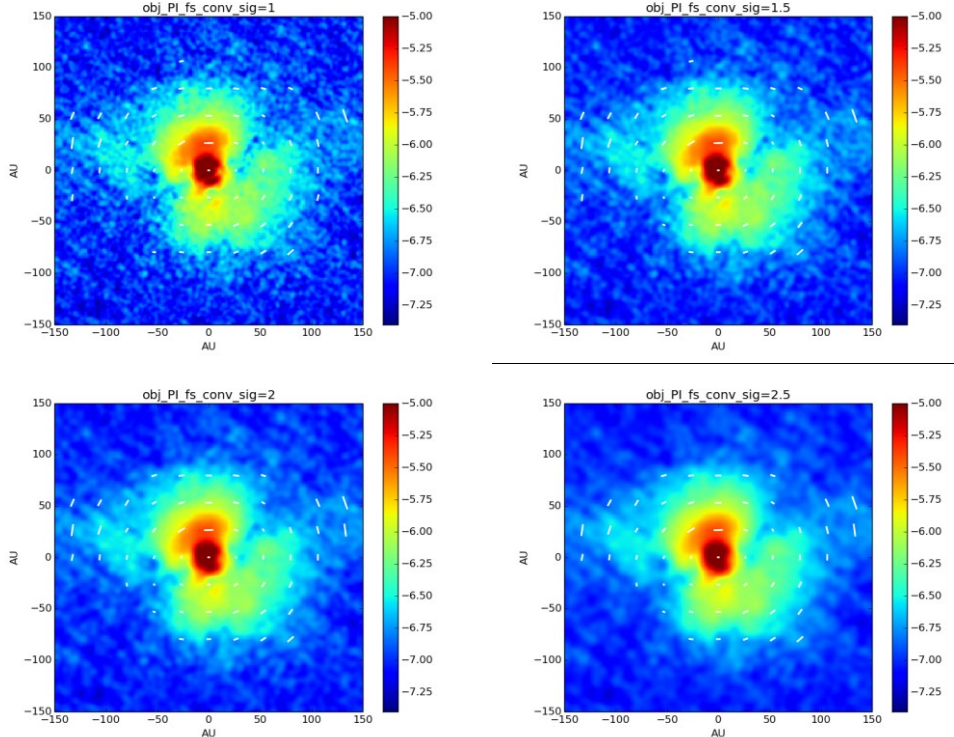


Figure 2.17. Convolved images of SU Aur with various sigma after flux scaling. Polarization vectors are also overlaid on the PI image.

>STEP 11: PSF realignment

By using imexam in IRAF, it was found that images shifts relative to their center. The shifts (at most 8 pixels), as shown in the figure below, were significantly larger than the angular resolution (~5 pixels) and hence made the stacking unreliable.

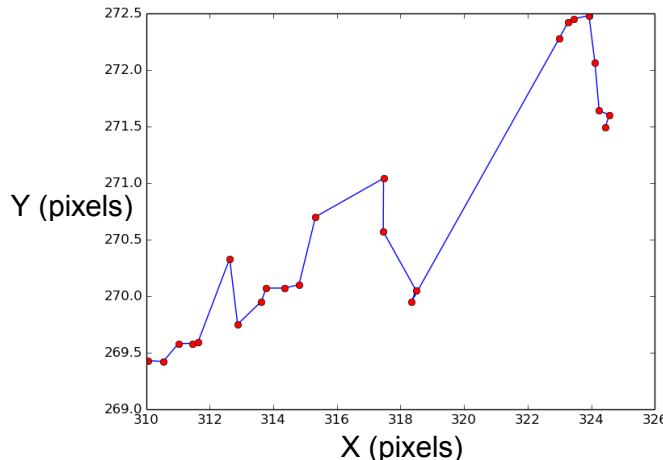


Figure 2.18. The stellar position in different exposures.

To compensate for this, the rotated images ($*_{rotl}.fits$) images were realigned by a value ($x_{\text{new}}, y_{\text{new}}$) relative to the predefined image center (271,318) arbitrarily chosen in Figure 2.18. The (X_i, Y_i) values in each images measured using imexam were saved into `center.txt` file. The file was then scanned to set alignment of new images shifted using imshift. The aligned images were then named as $*_{rotla}.fits$ found in the `aligned_I` inside `rotated_I` folder. After

realignment of intensity images, steps 8 to 10 were carried out again. For example, the new stacked Q and U images (`*_medQa`, `*_medUa.fits`) were generated using the aligned rotla images (see `8align_rotQUa.py`, `9median_QUa_set.py`).

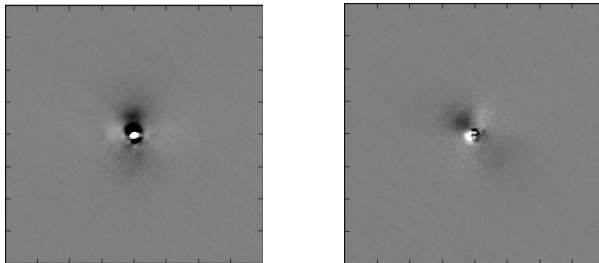


Figure 2.19. Left: realigned Q image (obj_{rot}Qa); Right realigned U image (obj_{rot}Ua). These images were used to make new PI images of the object (obj_{PI}a) as shown in the next figure.

From the Q and U images above, a butterfly pattern is apparent which is interpreted as polarized emission coming from light that was scattered on dust grains on the surface layer of the protoplanetary disk surrounding SU Aur. Such a pattern is a manifestation of tangential polarization vectors (Quanz et al. 2011). The pattern in the U images is rotated by roughly 45° compared to the Q images.

The new PI images were generated by using the `*_medQa` and `*_medUa` (realigned) as inputs eventually yielding ‘obj_{PI}a_{fs}’ image (see `test_Pi.py`, `test_Pi_fs.py`, and `Pi_set.py`). The PI images of ND1, object, and ref are shown below.

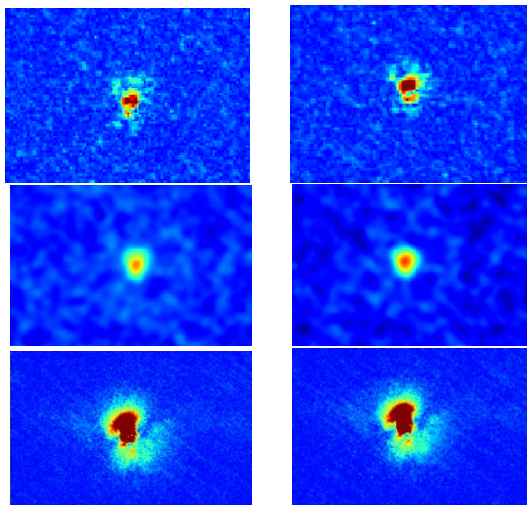


Figure 2.20. Left column: before realignment; Right column: after realignment of PI images. Row 1: PI image of ND1 set (ND1_{PI}a); Row 2: that of ref star (ref_{PI}a); Row 3: that of obj/ND10 (obj_{PI}a).

>STEP 12: Polarization vector mapping

This step entails mapping the polarization vectors of starlight that reflected from the disk. The resulting centrosymmetric pattern of the polarization of starlight verifies that disk and the dust in the vicinity of the object is illuminated by the same source. The output images are also inside `flux_scaling` folder (see `test_pol_vec.py` and `12PI_fs_conv_polvec.py`).

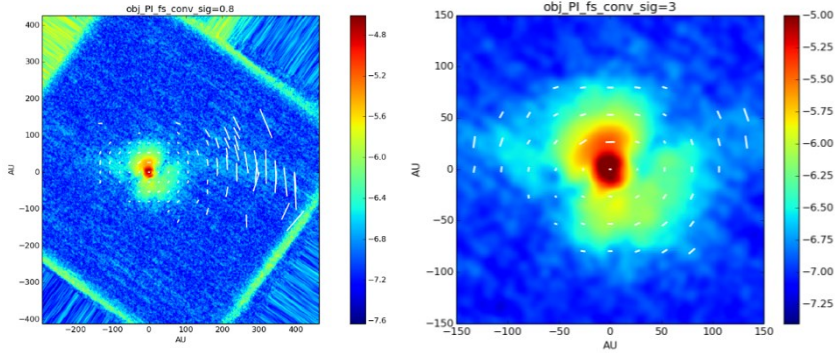


Figure 2.21. Polarization vector mapping of the flux scaled PI image in the outer regions (left) and inner regions (right).

>STEP 13: Minimizing background noise (subtracting median)

To better reveal the feature associated with the tail, another background subtraction was done. This was done by simply subtracting the median of the image (since the median represents the random noise in the PI image). The noise is of the order of 10^{-7} in PI/I_* .

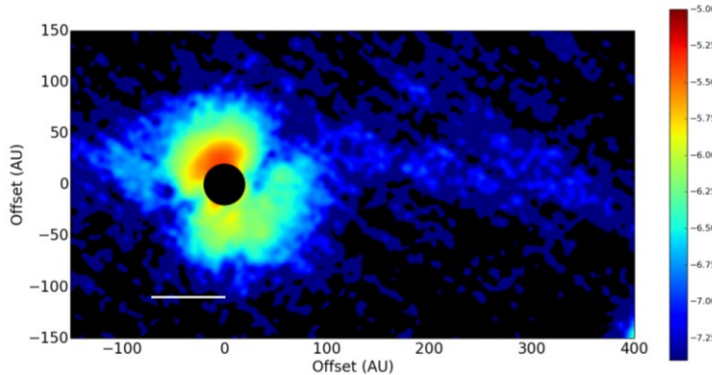


Figure 2.22. Final PI image after subtracting remnant background noise. The filled black circle is a software-added aperture mask with radius = $0''.15$ (~ 21 AU) to hide the saturated region within which data is unreliable.

>STEP 14: Measurement of disk geometry

This step entails the measurement of relevant physical quantities related to the disk like semi-major axis and inclination. The final PI image is overlaid with labels viewed using python default viewer and then manually saved in .png file format (see 14cmap.py). The final figures are saved in the `final_figs` folder (see `16final_ellipse_center_contour_scale_PA0.py`, `16final_polvec_ellipse_mask.py`, `16final_polvec_scale_PA0.py`).

Contour mapping

To assess the geometry of SU Aur's disk, isophotal lines of given fluxes in the scaled PI image were fitted. The outermost contours, defined by the minimum PI/I_* value (-6.75 in log colorbar = $\sim 5.6 \times 10^6$) were used as guide to fit an ellipse by a simple visual approach. Note that any objective approach to fit an ellipse would be inappropriate due to SU Aur's complex disk geometry.

Previously, a different approach was used to determine the major axis of the disk. The 1D flux (vertical profile at the image center) at a given position angle (0-180) was measured and then plotted the flux on a log scale compared with the all the other fluxes. The image was rotated at various position angles (PA's) to see at which PA has the widest flux broadening profile which corresponds to the major axis of the disk (see `13flux_PA_bulk.py`).

Ellipse Fitting

Elliptical fitting of the disk in the PI image yielded angular separations of major and minor axes: 1".2 and 0".90 (~170 AU and ~130 AU) at the apparent PAs $\sim 15^\circ$ and $\sim 60^\circ$, respectively. The geometric center of the fitted ellipse was offset by ~ 4.2 AU which is consistent with SU Aur's position within errors. The dimensions of the fitted ellipse represent the lower limit of the dimensions of the disk in PI.

Estimation of inclination

The inclination of the disk can be constrained to first order via the ratio between the width (minor axis of the projected ellipse) of the disk ($\sim 0.9''$) and the height (major axis of the projected ellipse) of the disk (1."2). This technique works in the assumption that the disk is intrinsically symmetric about the center. Hence, the apparent elongation of the minor axis is the effect of the viewing angle.

$$i = \frac{\text{minor axis}}{\text{major axis}} = \left(\frac{100 \text{ pixels}}{130 \text{ pixels}} \right) \frac{180^\circ}{\pi} \approx 40^\circ$$

Converting PI flux units

A number of databases were consulted to look for signs of disk in their SU Aur data.

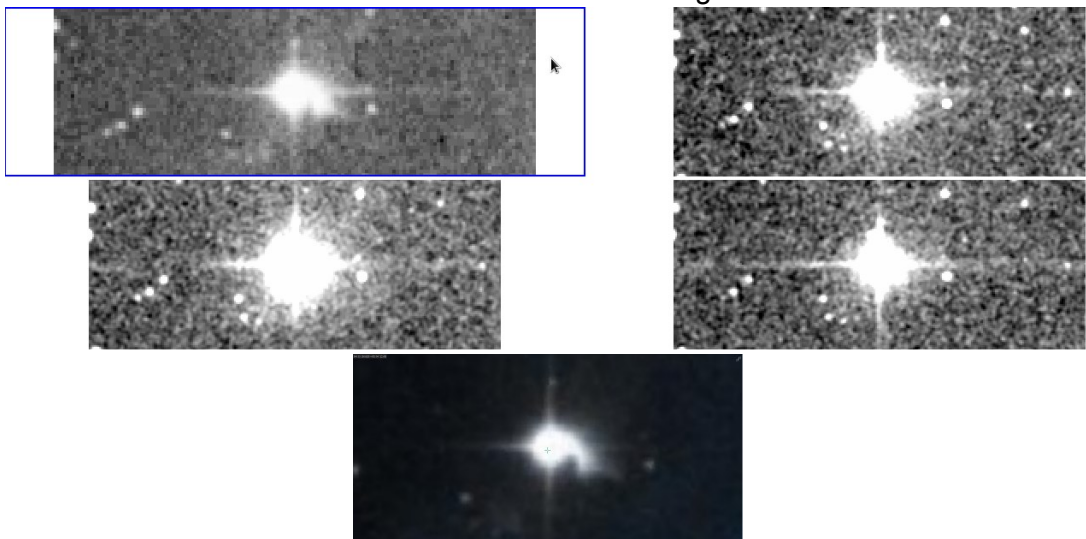


Figure 2.23. NIR images of SU Aur obtained from online databases: DSS (frame1), 2MASS J-band (frame 2), H-band (frame 3), K-band (frame 4). Bottom: image obtained from Simbad³. The extended structure (tail) is more apparent in this image. FOV: 2.53'

Magnitude measurements are also available in Simbad database. In particular, the H-band magnitude was used to convert the flux into micro-Jansky (μJ) unit using the FluxUnitConverter program developed by Hiro Takami-san. It requires just the wavelength band (H-band) and magnitude (6.558 mag according to Simbad) as inputs. So the flux of SU Aur is **2.50 J.**

³ Simbad: <http://simbad.u-strasbg.fr/simbad/sim-fbasic>.

Available data : [Basic data](#) • [Identifiers](#) • [Plot & images](#) • [Bibliography](#) • [Measurements](#) • [External archives](#) • [Notes](#) • [Annotations](#)

Basic data :

HD 282624 -- Variable Star of Orion Type

query around with radius arcmin

Other object types:	Or* () , * (HD,AG,BD,GCRV,GSC,HIC,HIP,JPl1,PPM,SAO,TYC,UCAC2) , X (2E,1RXS,XEST,[GBA2007],[SW98]) , IR (AKARI,IRAS,2MASS,WISE) , V* (AN,V*,AVSO) , Bm* (HBC,[KW97])	Interactive AladinLite view
ICRS coord. (ep=J2000):	04 55 59.38527 +30 34 01.5190 (Optical) [25.37 13.98 0] A 2007A&A...474..653V	
FK5 coord. (ep=J2000 eq=2000):	04 55 59.385 +30 34 01.52 (Optical) [25.37 13.98 0] A 2007A&A...474..653V	
FK4 coord. (ep=B1950 eq=1950):	04 52 47.84 +30 29 19.7 (Optical) [146.71 80.72 0] A 2007A&A...474..653V	
Gal coord. (ep=J2000):	172.5167 -07.9327 (Optical) [25.37 13.98 0] A 2007A&A...474..653V	
Proper motions mas/yr [error ellipse]:	1.18 -22.24 [2.89 1.59 0] A 2007A&A...474..653V	
Radial velocity / Redshift/ cz:	V(km/s) 23.20 [2.8] / z(~) 0.000077 [0.00009] / cz 23.20 [2.80] (~) C 2006AstL...32...759G	
Parallaxes mas:	6.85 [2.33] A 2007A&A...474..653V	
Spectral type:	G2III C 2009A&ARv..17...251S	
Fluxes (6):	B 10.33 [0.06] 2000A&A...355L..27R V 9.30 [~] C 2002yCat.2237...0D R 9.17 [~] E 2003yCat.1289...0Z J 7.199 [0.020] C 2003yCat.2246...0C H 6.598 [0.020] C 2003yCat.2246...0C K 5.990 [0.023] C 2003yCat.2246...0C	

Figure 2.24. Simbad database as source of H-band information of SU Aur.

>STEP 15: Radial PI distribution fitting

To compute the radial PI distribution power law, the PI distribution along the major axis of the disk was extracted and then plotted in a log-log plot and then fitted with a power law. First, the image was rotated vertically along P.A.=15° (major axis). The data points of the radial flux from the boundary of the mask (inside of which the data is unreliable) outwards were exported and then plotted using a spreadsheet, Microsoft Excel 2013, utilizing its built-in plotting and fitting functionality. The derived exponents of fitted equations determine the power law (see `15radial_PI_dist.py` and `15radial_PI_dist_combinedplots.py`)

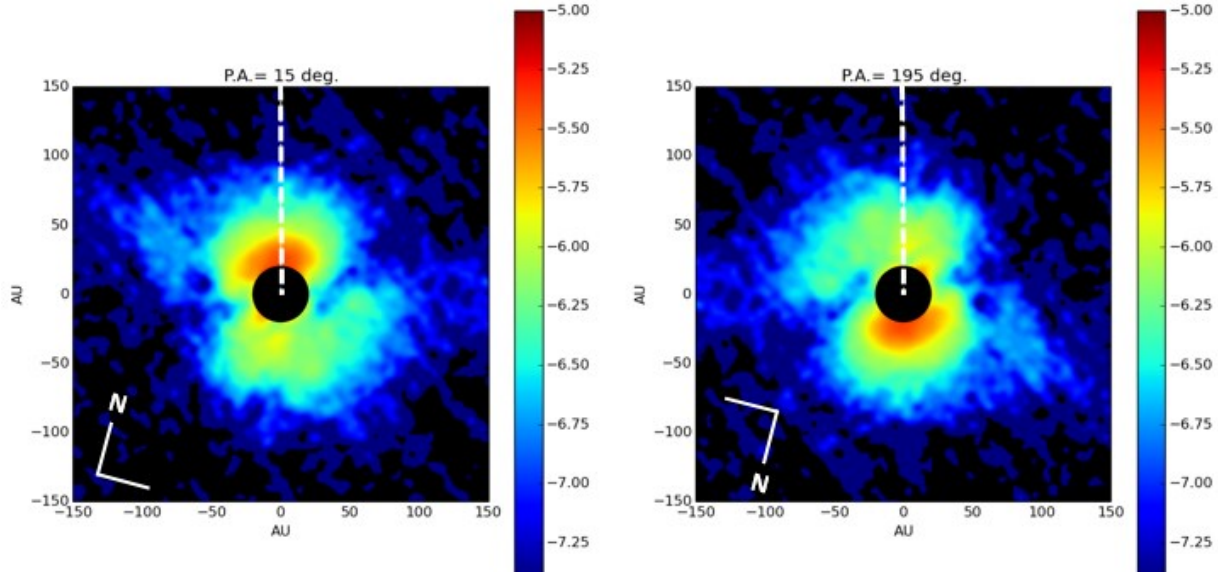


Figure 2.25. Rotated PI images wherein normalized PI values were extracted along the vertical above the mask for radial distribution fitting.

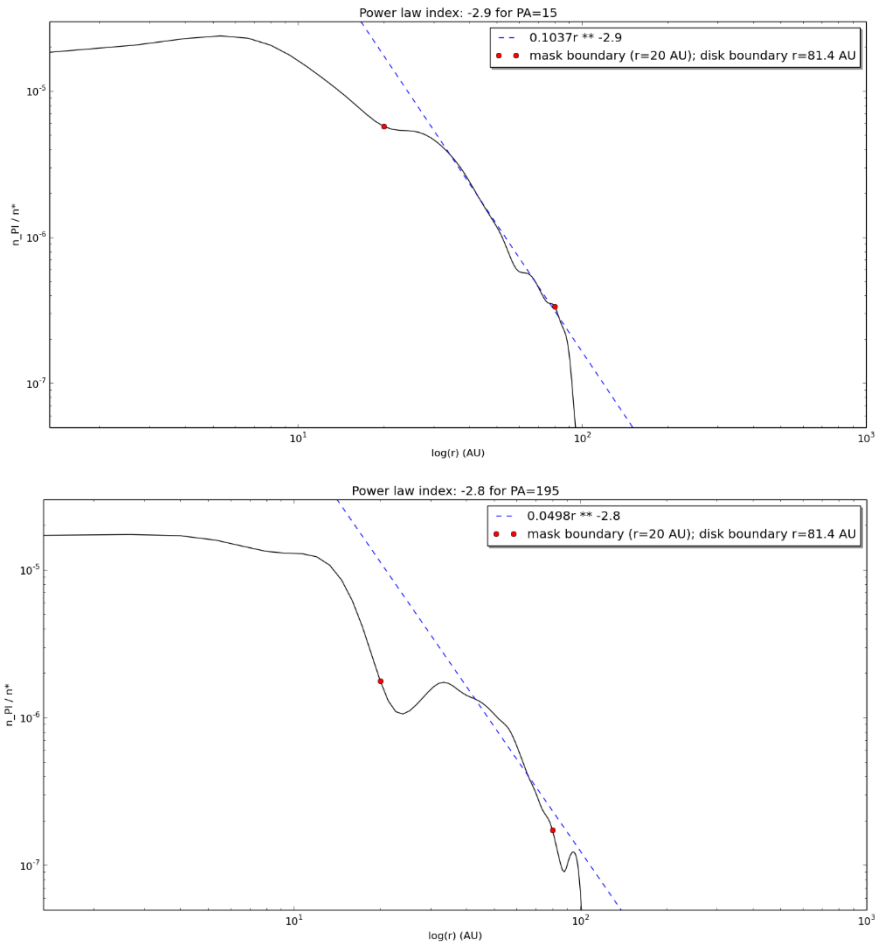
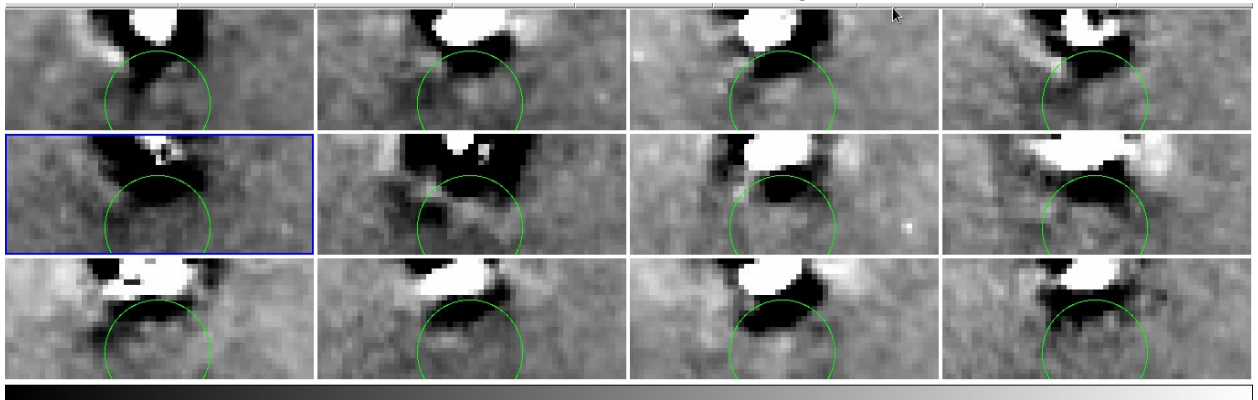


Figure 2.26. Top: radial PI distribution for $\text{PA}=15^\circ$ with fitted power law having index -2.9. Bottom: same plot but for $\text{PA}=195^\circ$ having index -2.8. The red dots denote the end points (mask radius and outer disk radius) where fitting was done. This range was adjusted such that it would yield better fit.

From the radial PI plot above, there was an apparent dip in the flux along $\text{PA}=195^\circ$. This dip was investigated by looking at the original Q and U images and zooming in to the same position in the individual images. The dip in the final PI/I_* image was then regarded as artifact since the dip feature was not consistent in each Q and U image.



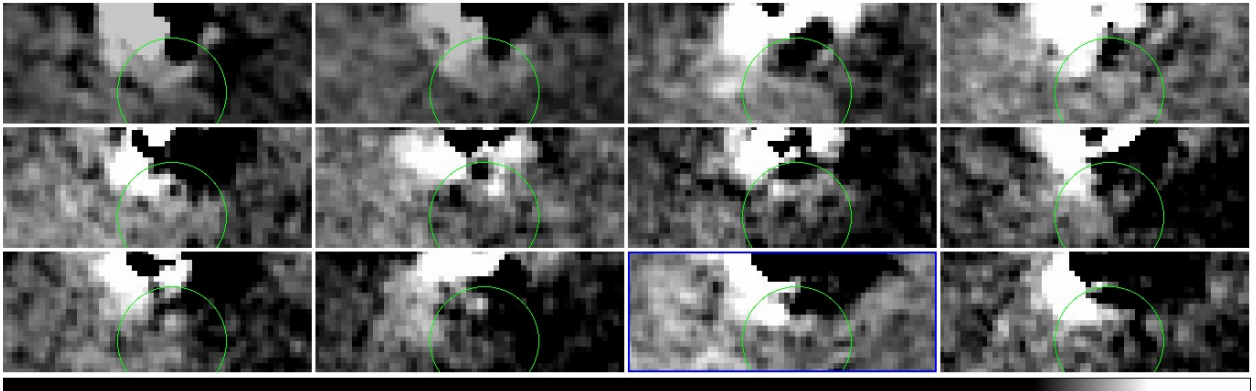


Figure 2.27. Investigating Q and U images to verify the anomalous dip in the final PI image at PA=195° below the mask.

II. Monochromatic simulation with conventional disk model

Table 2.2 shows the measured parameters from the observations and to be derived parameters in the simulations later. The simulation makes a set of images (3 usually) for β , h_0 , and ρ_0 . We used a resolution of 10^7 photons for each case. The resultant images for the Stokes parameters Q and U were convolved with the PSF of the reference star before obtaining the PI image using $PI = \sqrt{Q^2 + U^2}$. Then the PI flux is normalized to the stellar flux I^* , and scaled to match the pixel size of Subaru-HiCIAO.

Table 2.2. Dust and disk parameters for modeling in Sprout Code

Measured Parameters	
Parameter	Value
Viewing angle (i)	40°
Disk size	Inner radius: 21 AU Outer radius: 115 AU
Distance	140 pc
Derived Parameters	
Flaring parameter	-
Disk scale height	-
Density	-

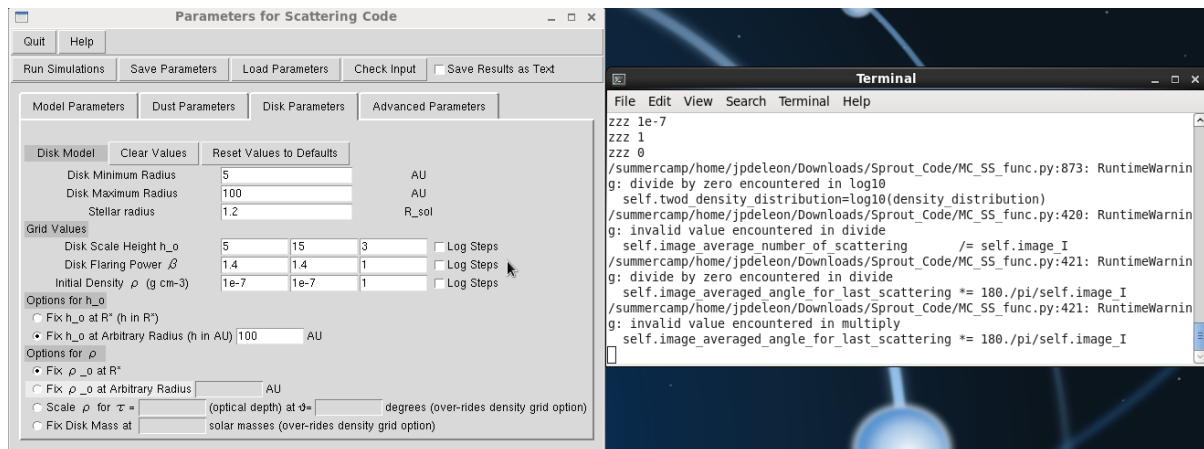


Figure 2.28. A snapshot of modeling GUI of Sprout Code.

CHAPTER 3

RESULTS

Observed PI Distribution

The normalized PI image of SU Aur in log stretch is shown Fig.3.0. The scaled flux is logarithmic over two orders of magnitude and north is up and east is to left. The disk can be traced in H-band from $\sim 0''.15$ to $0''.80$ ($\sim 21 - 115$ AU) from the star assuming $d=140$ pc. The total PI of the disk at $0''.15 < r < 1''.20$ is _____ mJy which is _____ % of the integrated stellar intensity. The total PI at $1''.20 < r < 2''.50$ along the tail is _____ mJy.

Moreover, a nonaxisymmetric illumination northeast of the disk (referred as the bright region) at $r \sim 0''.25$ (~ 35 AU, PA= 15°) from the star was also detected. The flux of the bright region peaked at $11.25 \mu\text{Jy pix}^{-1}$ ($\sim 1.28 \text{ mJy arcsec}^{-1}$). This is brighter than that in the other side exactly opposite along the major axis (referred as dim region) by a factor of ~ 2 ($F_{\text{PI}, \text{bright}} / F_{\text{PI}, \text{dim}} \sim 2$).

Disk Geometry and Orientation

To assess the geometry of SU Aur's disk, isophotal contours of given fluxes in the PI image were fitted. The outermost contours, defined by the minimum signal ($n_{\text{PI}}/n_{\text{L}*} \sim 5.6 \times 10^{-6} = 14 \mu\text{J}$), were used as guide to fit an ellipse by a simple visual approach. We note that using any objective approach to fit an ellipse would be inappropriate due to SU Aur's complex disk geometry.

Elliptical fitting of the disk in the PI image yielded angular separations of major and minor axes: $1''.2$ and $0''.90$ (~ 170 AU and ~ 130 AU) at the apparent P.A.= $\sim 15^\circ$ and $\sim 105^\circ$, respectively yielding an inclination $\sim 40^\circ$. The geometric center of the fitted ellipse was offset by ~ 4.2 AU which is consistent with SU Aur's position within errors. Note that this disk is not seen in the optical image in Jeffers et al. (2013). These results are further verified with the analysis of the centrosymmetric PI distribution of the disk as discussed in the following subsection.

We note, however, that it is still possible that the true disk inclination would be somewhat different from the computed value as we used contours of the same PI flux values for the ellipse fitting. These regions might not necessarily exhibit identical PI fluxes, as shown by the nonaxisymmetric bright region, on the disk surface as the PI flux depends on the scattering properties of the dust grains on the disk surface.

Resolved structures

Possible Asymmetric Spiral Arms

In Figure 3.0, PI emission in the southwest and northeast shows marginal extension from the ellipse, like spiral arms (hereafter S1 and S2, respectively). S1 is wider and brighter by about a factor of 2 than S2 ($F_{\text{PI}, \text{S1}} / F_{\text{PI}, \text{S2}} \sim 2$). The location of the spirals are contained within the fitted ellipse and only small portions of S2 protrude the outer part of the disk, as seen in Fig. 3.1. Both of the arms have the same rotation sense. If they are trailing structures as expected for spiral density waves, the rotation of the disk and any companions associated with the arms is counter-clockwise.

Tail associated with the Disk

Moreover, we have resolved a long tail associated with the disk extending westward at least $2''.5$ (~ 350 AU) across. Jeffers et al. (2013) described this feature as nebulosity seen in the optical extending westward at least 500 AU across.

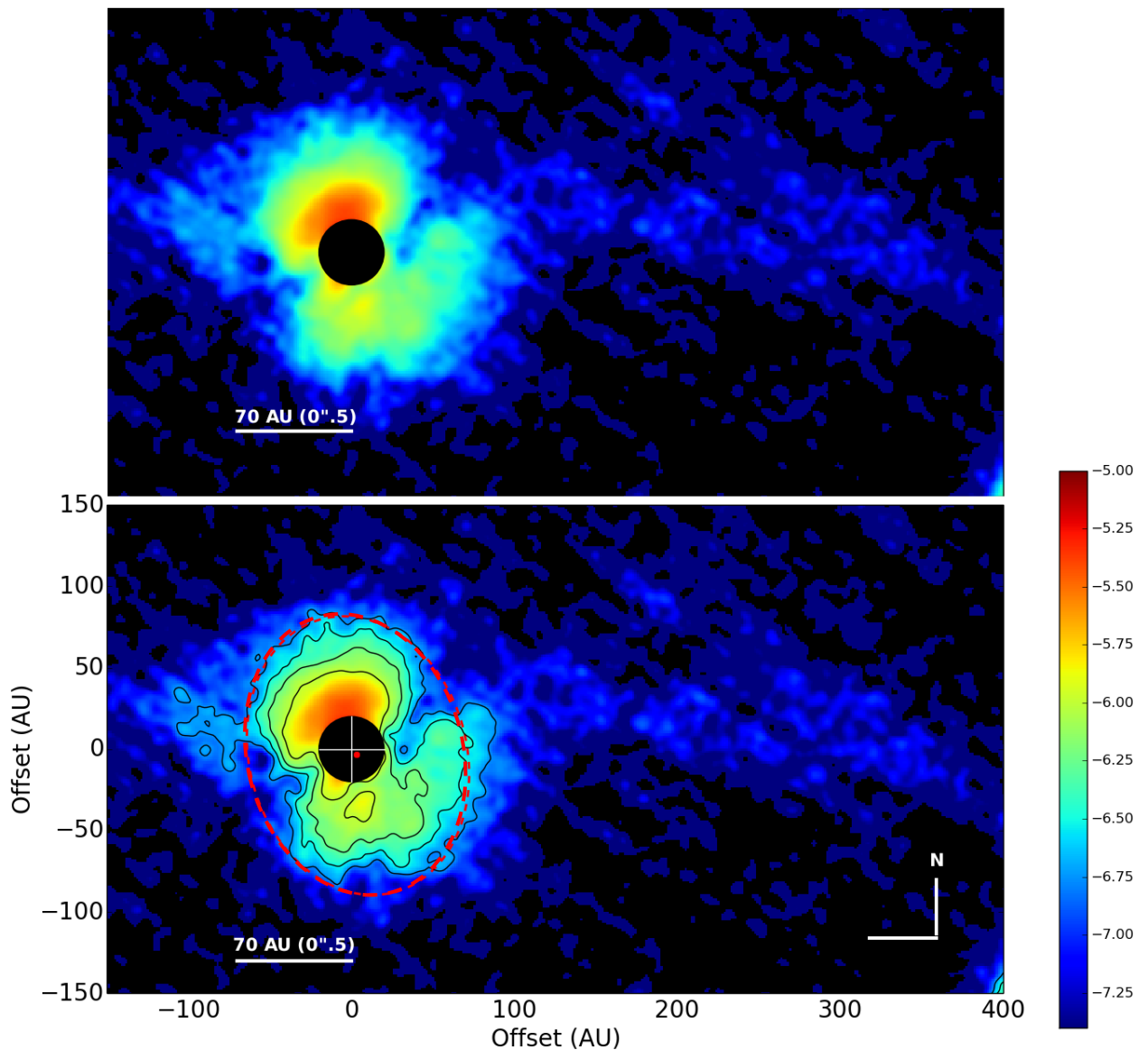


Figure 3.0. Final PI image (top) with labels shown (bottom). Isophotal contours was used to fit an ellipse to estimate the angular separation of the major and minor axes which are $1''.2$ and $0''.9$ (~ 130 and 170 AU), respectively. This implies that the disk is inclined $\sim 40^\circ$. The red dot indicates the offset of the fitted ellipse from the star's position.

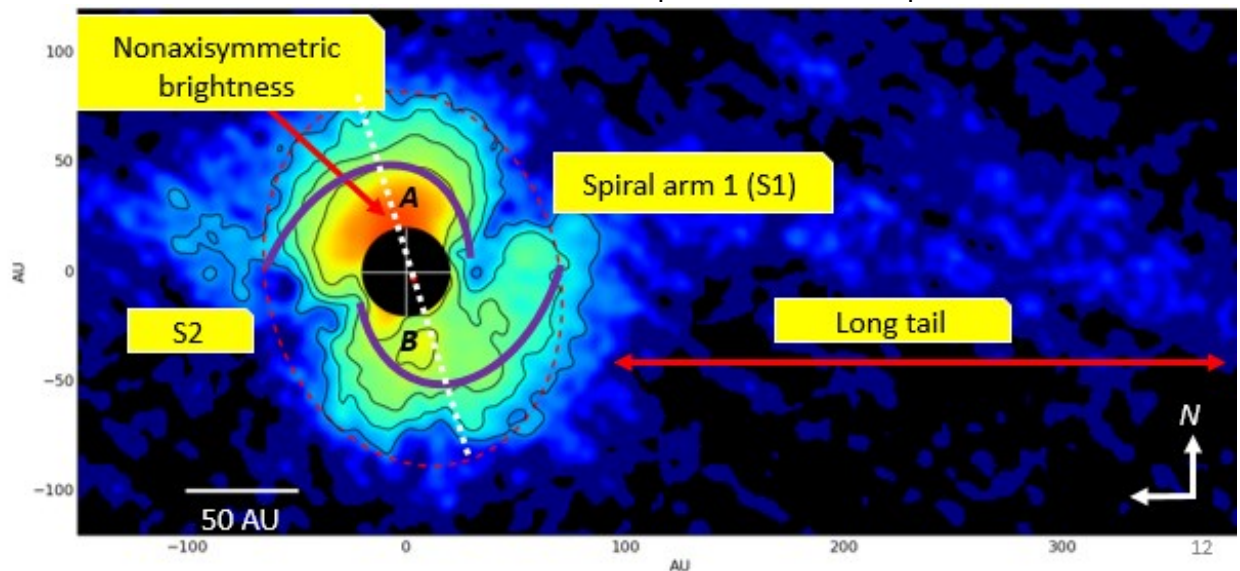


Figure 3.1. Resolved features in the final PI image of SU Aur. Objects are overlaid for clarity.
[24]

Polarization Fraction

The polarization vector map overlaid on the PI image are scaled to represent the degree of polarization of starlight that reflected from the surface of the circumstellar material. It shows a centrosymmetric pattern, as has been observed in several other disks using the technique of near-infrared imaging polarimetry (e.g., Hashimoto et al. 2011), indicating that the disk and tail are really scattered light that from the same source. A region of reduced polarization intensity along PA=60° and 240° aligned with the projection of the disk's minor axis was also identified. Moreover, the disk has low fractional polarization (<5%) than the tail (5 - 30%). This is because the total intensity of the star dominates in the inner disk region than that in the outer region. Essentially, the disk is more susceptible to contamination from the PSF halo of the star in the / flux distribution than the tail. Hence, the vectors are represented by the lower limit of the true degree of polarization. Note that polarization vectors show only the orientation and not the direction.

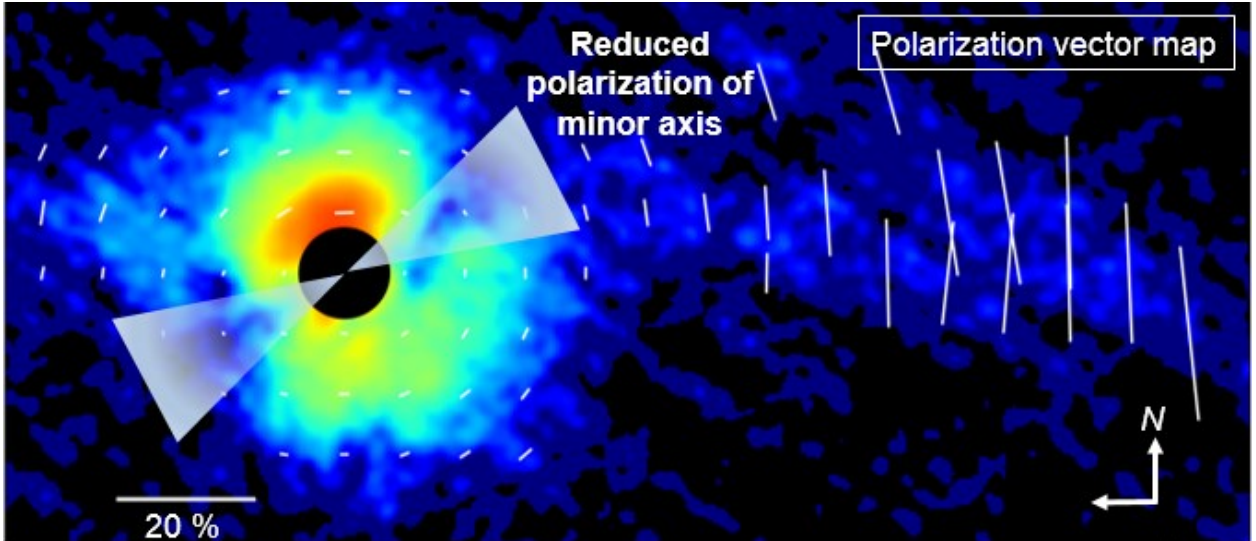


Figure 3.2. Vector map superposed to the PI image showing degree of fractional polarization. Triangles denote the opening of the apparent deficit in flux along the minor axis of the disk.

Radial PI Profile

Like in other SEEDS studies of young stellar objects (YSO) disks, we first extracted the radial PI profiles by averaging the flux across an 11-pixel wide strip along the major axis of the disk from the boundary of the mask until the disk's edge on both sides of the star. The width of the strip ($\sim 0''.10$) is chosen such that it is greater than the PSF FWHM. Then, a power-law function was fitted on each of the profile, as shown in Fig. 3.3. Between $0''.15$ and $0''.80$ ($\sim 21\text{-}115$ AU), the following power-law exponents that best fit the observed PI profiles were derived: -2.9 and -2.8 at PA=15° and PA=195°, respectively. Note that the radial profiles along the minor axis were not reported because of the deficit of PI flux.

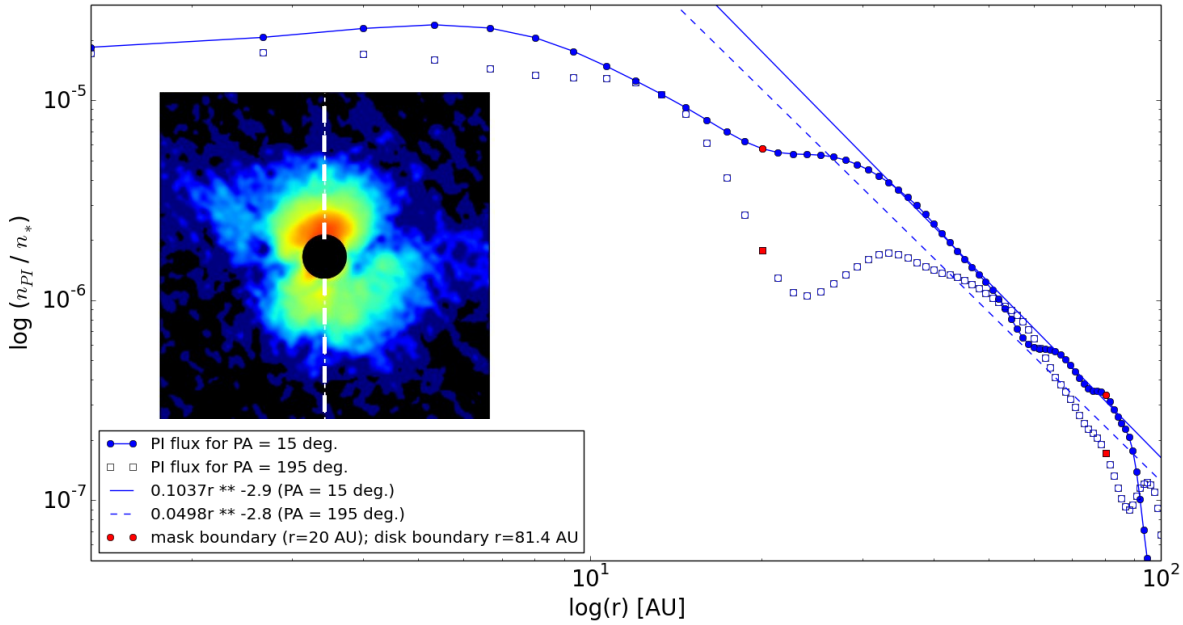


Figure 3.3. Radial PI profile along two sides of the disk. Filled circles represent extracted values along PA=15° with power law fit ($r^{-2.9}$) shown by solid line. Unfilled squares represent extracted values along PA=195° with power law fit ($r^{-2.8}$) shown by the broken lines. The red dots represent the boundary of the mask on the left and the end of the disk at the right.

DISCUSSION

Different Brightness at two sides of the disk

The different brightness observed at the either sides of the disk along the major axis may be due to nonaxisymmetric distribution, as discussed in some disks (e.g. Takami 2013, 2014).

Observed Structures

Possible spiral arms observed in the inner region of the disk as shown above may be explained by either the following:

- (1) spiral features possibly formed due to dynamical interaction between disk and an unseen companion, or even interaction with another star in the past;
- (2) spiral pattern might be produced by an infalling material (Tang et. al 2012).

The case of SU Aur therefore further demonstrate that SAO 206462 (Muto et al. 2012) and MWC 758 (Grady et al. 2013) may not be unique in hosting spiral arms. Moreover, like SAO 206462 and MWC 758, there is no indication of a cleared zone (= a disk hole) at H-band at $r=0''.20$ (~ 30 AU).

Depolarization of the Minor axis

The observed deficit in the flux along the disk minor axis can be attributed to two scenarios. On one hand, it can be due to scattering properties of dust grains that intrinsically produce reduced flux along the minor axis since the observed scattering angle deviates from 90° (i.e. geometric scattering problem). On the other hand, it can be a true feature due to a real structure (gap) in the disk caused by the opening of spirals. This feature is not an artifact because the difference in surface brightness between the dip in the opening of spirals and the rest of the disk is statistically significant and not within error bars. The PI vector map, being asymmetric along the minor axis, indicates that the second case is a more likely scenario.

Comparison to Other SEEDS Disks

Five YSOs with disks observed during the SEEDS survey was used for comparison. The representative samples show diverse disk morphologies such as gaps, annular rings, holes/dips, and asymmetries as shown in the beginning of this paper.

Brightness and Size of disk

SU Aur's disk is the brightest among the disk. It is at most brighter than 2M J1604 by a factor of 2. In terms of size, it is difficult to determine as other disks have smaller inner and bigger outer rings with gap in between.

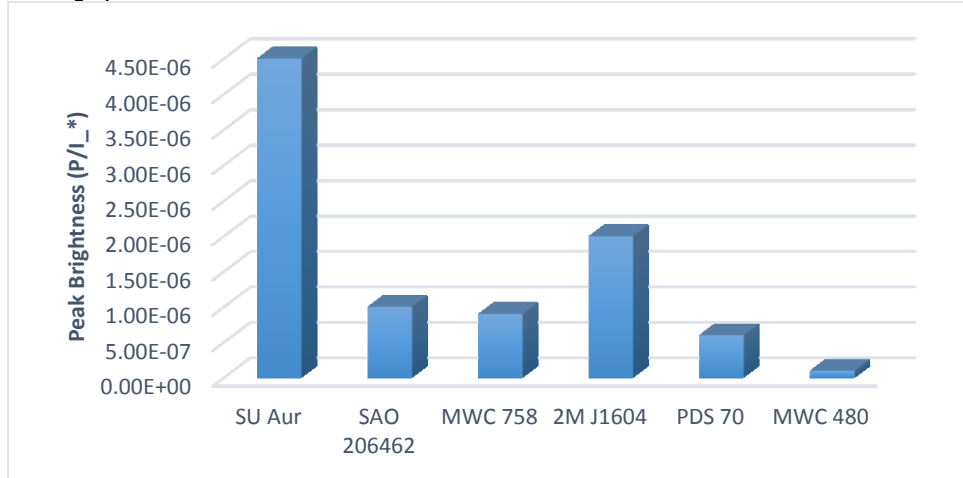


Figure 3.4. Comparison of peak brightnesses (normalized to their respective stellar fluxes) of SEEDS disks where SU Aur is the brightest among them.

Table 2.3. Disk measurements of SEEDS disks.

Object	Disk sizes/ radii (AU)	P.A. (°)	Inclination (°)
SU Aur	> 115 (20-80)	15	40
SAO 206462	40-140 (28-140)	55	11
MWC 758	60-200 (223-279: ~200)	65	21
2M J1604	40-63, (gap), 74-124	76	10
PDS 70	40-70-130 (28-210: ~137)	159	50
MWC 480	30-80-140 (27.4-137)	155	38

Disk Morphology

All the three significant features of SU Aur are not observed in any other single disk. The disks' dominant features are summarized in table 2.4. Possible spiral structures in the SU Aur's disk suggest that its morphology could be regarded as intermediate between MWC 758 (spiraled) and MWC 480 (uniform).

Table 2.4. Summary of observed morphology of SEEDS disks

object	Structures observed
SU Aur	Asymmetric brightness 2 spiral structures lying within 0."7 (~70 AU), and a tail associated with the disk that extends up to >2".5 (350AU)
SAO 206462	3 small-scale spiral structures
MWC 758	2 small-scale spiral structures at $r \sim 100-140$ AU; gaps
2M J1604	Ring; dip in outer disk elongated arc (50AU) extending over the disk inner hole (refuted)
PDS 70	Giant inner gap at $r \sim 70$ AU Ring
MWC 480	Uniform

Radial PI Distribution

The radial slopes are uniform in the neighboring regions close to the minor axis. Hence, the upper limit r^3 is used as a representative value. This slope, roughly, is observed in several

other HAeBe disks (e.g., Fukagawa et al. 2010; Quanz et al. 2011). From the five disks considered here for comparison, SU Aur's index is steeper except PDS 70 and 2MJ1604 with indices $p = -3.4$ and -4 (at least).

Table 2.4. Power indices describing the radial PI distribution of SEEDS disks.

Object	P.A. (°)	Power index
SU Aur	15, 105	-2.9, -2.8
SAO 206462	55	-2 to -5 (~ -3)
MWC 758	90, 270	-3.2, -2.8
2M J1604	55, 145, 235, 325	1.9 to 3.6, -4.7 to -4
PDS 70	159, 339	3.2, 2.9, -3.4, -3.8
MWC 480	150, 330	-2, -1.7, -2.8, -3.1

Possible Mechanisms for Non-axisymmetric Disk Distribution

Non-axisymmetric distribution of the inner disk region can be explained by several scenarios, including:

(1) Hot spots on the star;

(2) Shadowing by a nonaxisymmetric disk, including a puffed up inner rim (e.g. in South side);

(3) Clumpy accretion of dust and gas onto the star or inner wind associated with the star;
Less likely scenarios include:

(4) Obscuration by a companion star assuming SU Aur were a spectroscopic binary according to Bouvier (1986), or by a disk associated with a companion star (Watson & Stapelfeldt 2007; Wisniewski et.al 2008; Takami et al. 2013; Dullemond et al. 2003). The first case is possible because of SU Aur's intrinsic variability, as well as the third case since SU is known to be accreting (Calvet et al. 2004).

Disk Model Simulations

Complementary to observations, it is natural to perform disk simulations to derive relevant disk and dust parameters. To do this we carried out monochromatic radiative transfer calculations using Monte-Carlo code (a.k.a the Sprout code) specifically developed for use with SEEDS observations. The code was also used to reproduce and constrain RY Tau's disk parameters (Takami et al. 2013).

We used the dust model called KMH94, $R_v=3.1$ (ISM Model, Kim+94) with spherically symmetric homogeneous particles, using silicate and graphite. The density distribution of a standard accretion disk (e.g., Shakura and Sunyaev 1973; Lynden-Bell and Pringle 1974) is described in cylindrical coordinate (r,z) by:

$$\rho(r,z) = \rho_o \left[1 - \left(\frac{R_*}{r} \right)^{1/2} \right] \left(\frac{R_*}{r} \right)^a \exp \left[-\frac{1}{2} \left(\frac{z}{h} \right)^2 \right],$$

where where ρ_o is a constant to scale the density; R_* is the stellar radius; r is the radial density exponent; and h is the disk scale height. The scale height h increases with radius as $h = h_0 r^\beta$, where β is the flaring power ($\beta > 0$). According to more detailed models of disk structures by Chiang and Goldreich (1997); D'Alessio et al. (1999a), the scale height exponent varies with radius in the inner disk but follows a similar power law beyond a few AU (Cotera et al. 2001). In addition to the above parameters the minimum and maximum radii of the disk are included as free parameters. The gas-to-dust mass ratio is assumed to be 100.

Currently, disk simulation using measured parameters was unable to reproduce the observed morphology of SU Aur, including the nonaxisymmetric brightness, possible asymmetric spiral arms, and depolarization of minor axis. It is important to note that we use an axisymmetric

distribution of the circumstellar material for the simulations in this and following sections. This implies that, in principle, these simulations cannot reproduce the asymmetry at the PI distribution about the rotation axis of the disk (and the jet axis). Simulations for an asymmetric PI distribution are beyond the scope of this paper.

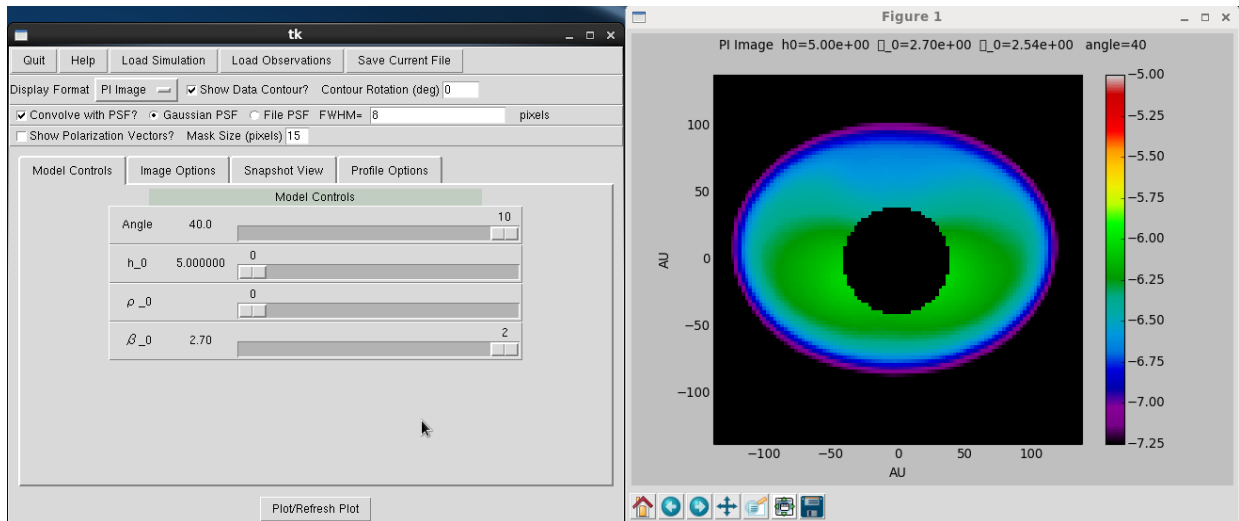


Figure 3.5. A sample simulation result with $i=40^\circ$, $h=5$, $\beta_0=2.7$ ($\rho_0=0$, fixed).

CHAPTER 4

SUMMARY AND CONCLUSIONS

We present high-resolution polarimetric imaging observation in H-band for the first time of the scattered light from the protoplanetary disk around the young stellar object SU Aur. Our observation reveals the presence of complex disk structure traced from $0''.15 - 0''.80$ ($\sim 21-115$ AU) from the star. Moreover, we have resolved possible asymmetric spiral structures lying within $r \sim 0''.7$ (~ 100 AU) located in the E and W of the star, and a tail associated with the disk that extends up to at least $2''.50$ (350 AU). The two asymmetric spiral structures and the tail associated with the disk are real features although we are still verifying the authenticity of nonaxisymmetric illumination of the disk in the inner region. Explaining the observed morphology call for many possible scenarios. In particular, embedded planet(s) capable of producing the spiral arms, as proposed in some objects, cannot be ruled out. In terms of disk morphology, we may consider SU Aur to be intermediate between MWC 758 (spiraled) and MWC 480 (uniform). This makes SU Aur an interesting target for future follow-up observations with SMA and/or ALMA.

FUTURE WORK

The tail has been observed and extensively studied in optical regime before. The analysis of the tail in NIR will still be done as a continuation of this project. In particular, the calculation of dust mass (and mass ejection rate of the tail) are currently in progress. It is useful to compare the results with millimeter data of SU Aur's disk, if it exists. For example if the near/far side of the disk/spirals is determined via CO observations, then we can determine if forward (yes if nearside is brighter)/backward (yes if farside is brighter) scattering by dust in the disk is preferred.

For the disk simulation, we will explore a wider parameter space to better constrain dust and disk parameters. It is possible that we have to consider alternative dust model in the future. Look into the possibility of interaction between the disk and unseen exoplanet is a possibility. Estimation of the perturber mass and location to account spirals as done in previous SEEDS papers should be done whenever possible.

ACKNOWLEDGMENTS

I express my gratitude to AS/IAA for the Summer Internship program including their support. I thank all the junior and senior researchers that best exemplified how real Astronomy research is done. I enjoyed all lectures, lunch talks, meetings, and gatherings throughout the program. Thanks to all my co-interns, you are my true friends. I hope we can become active collaborators in the near future. Above all, I express my deepest gratitude to my advisers, especially Dr. Hiro Takami for being my guiding light. Hiro-san had been so kind, caring, and extremely understanding. I owe him the success of this project. I look forward to working with him in years to come.

REFERENCES

- Acke, B., et al. 2004, A&A, **422**, 621
Akeson, R.L., et al. 2002, ApJ, **566**, 1124

- Bertout, C., Basri, G., & Bouvie, J. 1988, ApJ, **330**, 350
- Bertout, C. & Genova, F. 2006, A&A, **460**, 499
- Canovas, H., et al. 2013, A&A, **556**, A123
- Chiang, E.I. & Goldreich, P. 1997, ApJ, **490**, 368C
- Cotera, A., et al. 2011, ApJ, **556**, 958C
- d'Alessio, P., et al. 1998a, ApJS, **500**, 411D
- DeWarf, L.E., et al. 2003, ApJ, **590**, 367
- Grady, C. A., et al. 2013, ApJ, **762**, 48
- Hayano, Y., et al. 2004, Proc. SPIE, 5490, 1088
- Hashimoto, J., et al. 2011, ApJ, **729**, L17
- Hashimoto, J., et al. 2012, ApJ, **758**, L19
- Herbig, G.H., et al. 1952, JRASC, **46**, 222
- Hinkley, S., et al. 2009, ApJ, **701**, 804
- Hodapp, K., et al. 2008, SPIE, 7014, E42H
- Jeffers, V., et al. 2013, A&A, **561**, 1
- Johns-Krull, C.M. 1996, A&A, **306**, 803
- Joos, F., et al. 2008, Proc. SPIE, 7016, 48
- Kusakabe, N., et al. 2012, ApJ, **753**, 153
- Mayama, S., et al. 2012, ApJ, **760**, L26
- McCaughrean M.J., et al. 2000, Protostars and Planets IV, p.485
- Muto T., et al. 2012, ApJ, **748**, L22
- Muzerolle, J., et al. 2003, ApJ, **597**, L149
- Quanz, S. P., et al. 2011, ApJ, **738**, 23
- Takami, M., et al. 2013, ApJ, **772**, 145
- Takami, M., et al. 2013-12, ApJ, submitted [SCI]
- Tamura M., et al. 2006, Proc. SPIE, 6269, 28
- Tang, Y.W., et al. 2012, ApJ, **547**, A84
- Unruh, Y.C., et al. 2004, MNRAS, **348**, 1301

APPENDIX

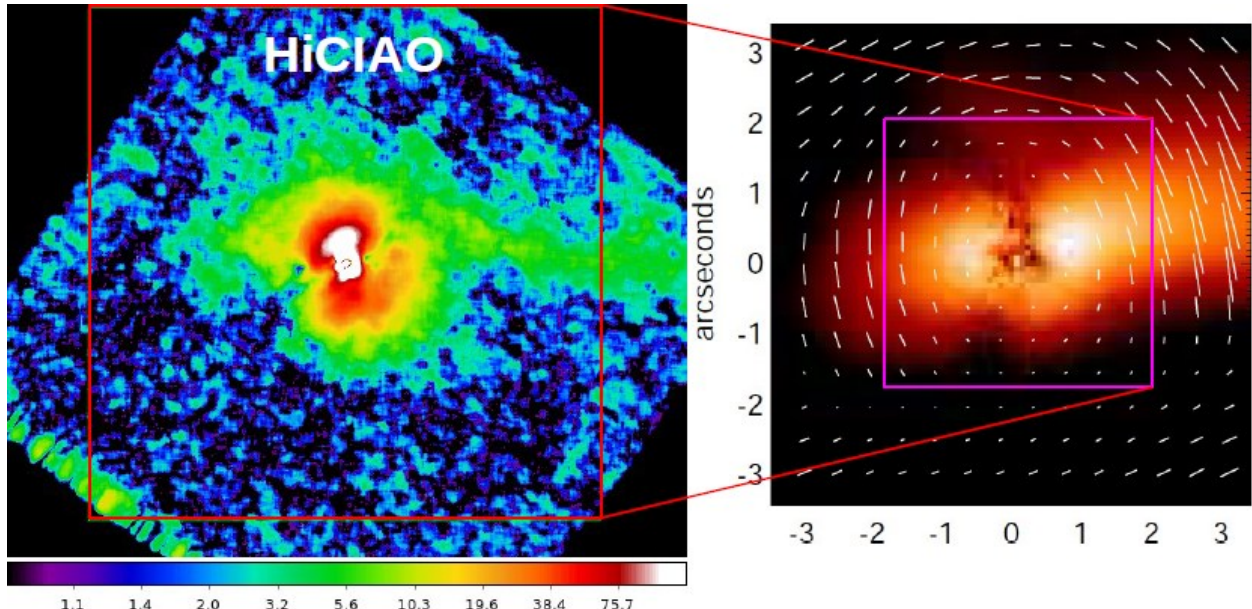


Figure A.1. The SEEDS quick-look image of reduced PI image of SU Aur (left), and optical PI image from Jeffers et al. (2013).

The HiCIAO Instrument

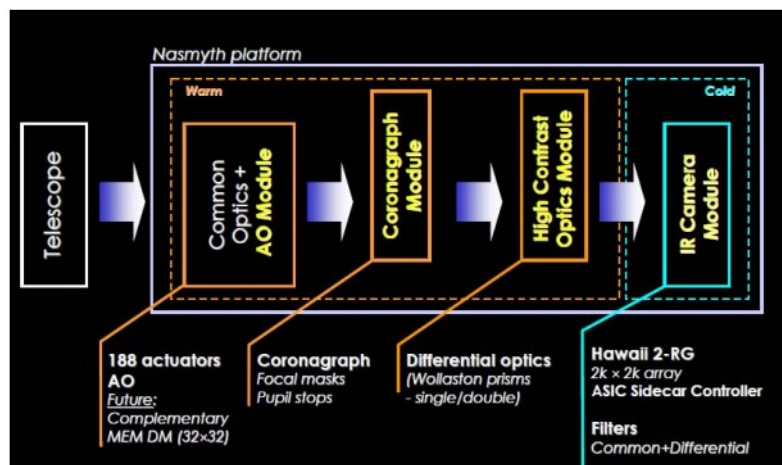


Figure A.2. Schematic diagram of the HiCIAO+AAO188.⁴

⁴ Lifted from “HiCIAO Performance Report for SEEDS.” Please refer to
http://www.naoj.org/staff/kudotm/SEEDSHiCIAOPVreport_final090923e.pdf
[32]

Optics Layout

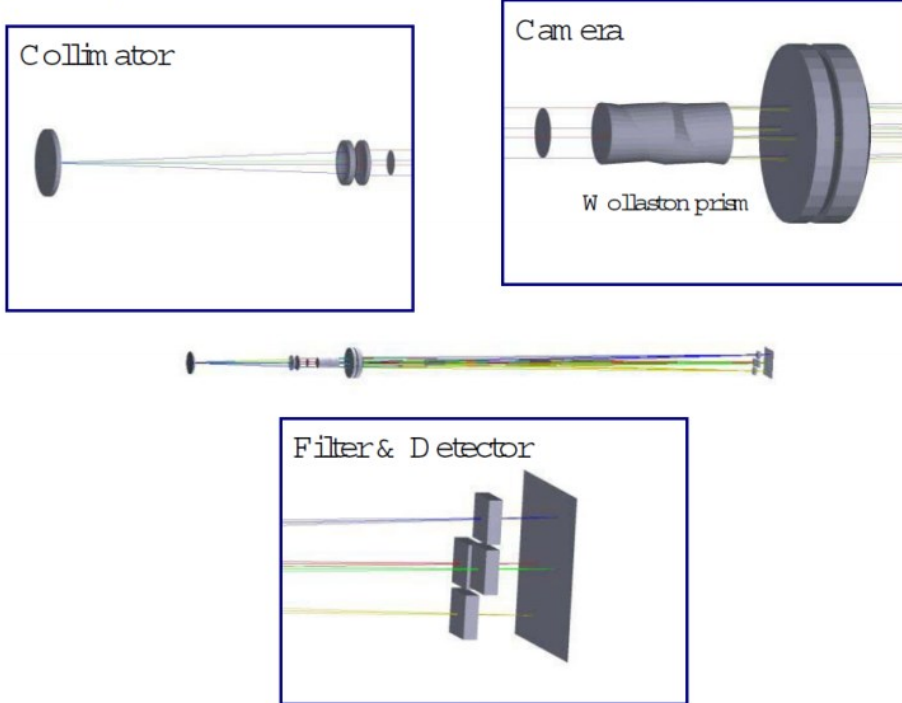


Figure A.3. Optics layout of HiCIAO.

Summary of HiCIAO Observation Modes:

Speckle subtraction: Differential Imaging

Angular Differential Imaging (ADI): on sky angle

Polarimetric Differential Imaging (PDI): Stokes QU

Spectral Differential Imaging (SDI): simultaneous imaging- at different wavelengths

Basic Principle: measure two observables of the source (quasi-)simultaneously, and derive exoplanet signal from difference image (stellar signal should subtract out, i.e. not vary for the observable)
=> in/out molecular absorption bands

Useful Unit Conversions

Rescaling the PI image in arcsec and AU units

>>Pixel to AU – unit conversion

[AU] = [Pixel] [pixel resolution= 9.53 mas/pixel] [distance of star in parsec (pc)]

For example, if the major axis (diameter) is measured as 170 pixels, so

$$(170 \text{ pixels}) * (0.0095 \text{ arcsec/pixel}) (140 \text{ AU/arcsec}) = 226.1 \text{ AU (4 SF)}$$

Therefore, the semi-major axis is about 115 AU

>>Pixel to arcsec – unit conversion

To know the number of pixels in a 0.3 diameter occulting mask,

$$[\text{pixels}] = [\text{arcsec}] / [\text{arcsec/pixel}]$$

$$(0.3 \text{ arcsec}) / (0.00953 \text{ arcsec/pixel}) = 31.5 \text{ pixels}$$

>>Arcsec to AU – unit conversion

To know the number of AU in a 0.3 diameter occulting mask,

$$[\text{AU}] = [\text{arcsec}] [\text{pc} = \text{AU/arcsec}]$$

$$(0.3 \text{ arcsec}) (140 \text{ AU/arcsec}) = 42 \text{ AU} \Rightarrow r = 21 \text{ AU}$$

Computing the pixel resolution of HiCIAO H-band images

Diffraction limit (angular resolution) of an optical system is defined as

$$\theta_{radians} = 1.22 \frac{\lambda}{D}$$

Given $\lambda = 1.65 \mu m$ (H – band, NIR), $D = 8.1 m$ (Subaru's effective diameter), and pixel scale of HiCIAO = 9.53 mas/ pixel

$$\theta_{arcsec} = 2.51 \times 10^{-7} \left(\frac{180 \text{ degree}}{\pi} \right) \left(\frac{60 \text{ arcminute}}{1 \text{ degree}} \right) \left(\frac{60 \text{ arcsec}}{1 \text{ arcmin}} \right) = 0.0519 \text{ arcsec}$$

Thus,

$$\frac{\text{angular resolution}}{\text{pixel scale}} = \frac{0.0519 \text{ arcsec}}{0.00953 \text{ arcsec/pixel}}$$

pixel resolution = 5.4 pixels

The Sprout Code

Sprout⁵ is a program to generate model images of scattered light from circumstellar disks, in multiple polarization states and viewing angles, and to quickly and efficiently compare those models to observational data. The program has two parts.

First, a GUI lets you set up a grid of models, varying the geometry of the disk. You can select the size of the simulation, the inner and outer radius of the disk, and the dust grain model, and a range of parameters for the density, flaring and scale height of the disk. The code runs quickly (~ 1 min per simulation), so it is possible to use it to explore parameter space.

Second, Sprout contains a viewing GUI. You can load a set of models, and easily and quickly scroll through parameter space and viewing angle to explore the morphology of the disk in I, Q, U, V and polarization intensity. Observational data can be displayed in contour, and there are viewing modes for radial profiles and the underlying density distribution of the model. The simulations can also be imported into other programs for further analysis, and FITS files for individual views can be exported.

⁵ Please refer to <http://www.asiaa.sinica.edu.tw/~jkarr/Sprout/sprout.html>